Modeling and Applications of Thermoelectric Generators

Abdulmohsen A. Alothman

Dissertation submitted to the Faculty of the

Virginia Polytechnic Institute and State University

in partial fulfillment of the requirements for the degree of

Doctor of Philosophy

in

Engineering Mechanics

Muhammad R. Hajj, Chair

Saad A. Ragab

Scott T. Huxtable

Surot Thangjitham

Mayuresh J. Patil

March 23, 2016

Blacksburg, Virginia

Keywords: Thermoelectric, Harvesting Energy, Organic Storage Devices, TEG Application

Modeling and Applications of Thermoelectric Generators

Abdulmohsen A. Alothman

(ABSTRACT)

We develop a simplified one-dimensional numerical model that simulates the performance of thermoelectric generators (TEG). The model is based on the energy and electrical potential field equations. The Seebeck coefficient, thermal conductivity, electrical resistivity and Thomson coefficient of the TEG material are used to predict the harvested power. Bismuth-telluride is used as semiconductors materials of the TEG, which is the most commonly used material by industry. Experiments on three TEG modules were performed to validate the numerical model. A comparison with predicted levels of harvested energy based on the TEG specifications is also performed. The results show differences between the experimental and numerical values on one hand and the predicted ones on the other hand. The reason for these differences are discussed. A procedure to estimate the sensitivity of the harvested power to different inputs and TEG parameters is detailed.

In the second part of the dissertation, we integrate a thermoelectric generator with an organic storage device. The performance of the integrated system for different values of load resistances and temperature gradients is determined. Finally, we demonstrate that power generated from a TEG is related to the flow rate in a pipe and can, thus, be used as a flow meter. Particularly, a dimensionless relation between the TEG's peak power and Reynolds number is determined.

Dedication

This PhD dissertation is dedicated to all members of my family, especially to my parents, siblings and wife.

Acknowledgments

First and foremost I would like to thank my advisor, Prof. Muhammad R. Hajj for his guidance and support. He provided me guidance, assistance, encouragement and expertise that I needed during my research. I would also like to thank my colleagues Mohammed Al-Haik, Mohamed Zakaria and Chris Denny whom have lent their knowledge, time and expertise to me while designing the experimental setups.

I am thankful to my parents Abdulrahman Alothman and Norah Alawad for their constant love, prayers and endless support. Also, my thanks are given to my brothers and sisters whom have constantly lent their time and support. I would like to thank my wife Reem Ibn Salamah for her love, support and understanding after she decided to join me into this journey. Finally, I am thankful to King Abdulaziz City for Science and Technology (KACST) for their support of this research.

Contents

List of Figures

List of Tables

Chapter 1

Introduction

In many applications, energy is lost in the form of hot exhaust gases or from hot surfaces. Developing recovery technologies of waste heat can enhance the efficiency of industrial processes or used to power other systems, small devices or sensors. One recovery technology is through using thermoelectric generators. A thermoelectric generator consists of two thermoelectric semiconductors (n-type and p-type) that are connected through conducting plates. When the plates are subjected to a temperature difference, the electrons and holes accumulate on the cold side. This accumulation results in an electric field between the cold and hot sides, which results in a voltage across the semiconductors and an electric current when adding an electric load. The phenomenon of converting a temperature difference to electric power is known as the Seebeck effect. Advantages of thermoelectric generators include their compact size and light weight. In addition to being reliable, they have low maintenance costs and long life spans. Consequently, they have been proposed as an alternative to batteries to power remote small devices or sensors.

In this dissertation, we develop a numerical model for performance prediction of the TEG, investigate the potential for integrating a TEG with an organic capacitor and present a potential application of TEG for remote metering of flow rate of hot water. The structure and organization of this dissertation are as follows:

- We introduce in Chapter one (this Chapter) the operation principle of TEG and describe the significance and motivation for this work.
- In Chapter two, we develop a simplified one-dimensional model to predict the performance of TEG modules. The model is based on the coupled energy and electrical potential field equations. Particular attention is paid to the temperature variations within the semiconducting material and its impact on the voltage and power generation. The model is then validated experimentally with three different TEG modules. The numerical prediction is compared with manufacturers' specifications. Finally, we perform uncertainty analysis to determine sensitivities to different input conditions.
- In Chapter three, we investigate the potential of integrating a TEG with a novel organic capacitor. Particular attention is paid to the effects of temperature difference and load resistance on the performance of the integrated energy harvested/storage system.
- In Chapter four, we demonstrate a potential application for the TEG as a water meter where peak power generated by the TEG from a transient flow of hot water is related to the flow rate.
- Finally, we present in Chapter five concluding remarks and future recommendations.

Chapter 2

A Simplified Model for Performance Prediction of TEG

2.1 Introduction

The large levels of heat losses from hot exhaust gases and surfaces have raised the interest in developing recovery technologies that can be used to power other systems, small devices and sensors. One technology that has attracted interest is thermoelectric generation. This technology is based on placing thermoelectric p-type and n-type semiconductors between conducting plates. When the two plates are subjected to different temperatures, the accumulation of holes and electrons on the cold side results in a voltage across the semiconductors. This voltage is an electricity source that can be used for different purposes.

There has been many investigations that showed potential implementation of energy harvesting in different fields. Anatychuk et al. [1] installed eight thermoelectric modules into gas and liquid heat exchangers which was a part of a 50-kW stationary diesel power plant. These modules harvested up to 2.1 kW which is around 4.4 % of the power plant output. Elefsiniotis et al. [2] placed thermoelectric generators on aft pylon fairings of an aircraft. These TEGs produced maximum and minimum energy levels of 81.4 J and 28.1 J, respectively. That amount of energy was estimated to be enough to power instruments such as sensors and monitoring devices, which can ultimately reduce maintenance costs. Data collected during regular flights showed the potential to harvest 69.78 J [3]. Power recovery from wasted heat of a blast furnace slag was modeled by Xiong et al. [4] with two-stage thermoelectric generators. Their predictions showed that 0.44 kW and 1.14 kW can be harvested for inlet temperatures of 100 ^{o}C and 150 ^{o}C, respectively. Liu et al. [5] built a prototype vehicle and attached a number of TEGs to its exhaust pipe. The temperature of the cold side was maintained by recycling water. The maximum power harvested from 60 modules was 944 W. Sun et al. [6] developed two-stage serial and parallel TEG models for an internal combustion engine. The two-stage model showed output power improvement that is higher than a single-stage at an operating hot temperature of 600 K. Using two modules and connecting TEGs electrically in parallel has been determined to have a better higher performance than the serial pattern. Cino [7] studied heat recovery from pizza ovens with a hot temperature of 200^{o}C. They were able to recover 13.2 % of waste-heat energy by using TEG modules.

In addition to the experimental studies, several numerical investigations have been performed. Wang et al. [8] developed a three-dimensional model of a single unit by coupling energy and

electrical potential field for a thermoelectric cooler. Their goal was to show the current effect on performance. Meng et al. [9] modified the model to use it for thermoelectric generators by guessing the initial and boundary conditions. They concluded that increasing the semiconductors cross-section area reduces the ambient heat loss from the sides. They also applied their numerical model to two-stage thermoelectric modules to study performance enhancement. It was found that the number of elements used in a hot stage device should be higher to increase the efficiency [10]. McCarty [11] compared two different numerical models, one-dimensional and three-dimensional, using ANSYS for thermoelectric cooler. He also validated his results experimentally using a thermoelectric module with 24 elements. The comparison showed the importance of including the Thomson coefficient in the model to predict the right performance. Chen et al. [12] modeled the performance of a single TEG with a three-dimension numerical model using FLUENT. The simulation software was used to estimate the electric field in computational fluid dynamics environment. By using a thermoelectric classical thermal resistance model, Gaowei et al. [13] improved the model to include the contact effects and how they impact power prediction. The contact resistance from tabs and heat sink can be parts of internal TEG resistance. Therefore, the optimum resistance at which the maximum harvested power is shifted.

A numerical model with two-dimensional thermal profiles was developed by Yang et al. [14]. The temperature profile was solved for by simplifying the energy equation with steady-state and the constant properties assumption. Accounting for the temperature distribution showed improvement in performance prediction. Reddy et al. [15] introduced an integrated thermoelectric generator whose performance was predicted using numerical simulation. The governing equations including

the continuity, momentum and energy equations coupled with non-Ohmic current-voltage relation were solved by using the finite volume method. Sahin et al. [16] studied the thermodynamic irreversibility of TEG and how it effects the power harvested. They concluded that operating at the optimum power reduces entropy generation rate. A three-dimensional TEG numerical model was presented by Bjork et al. [17] who investigated the internal heat loss effect on power harvested. The governing equations included the heat flux and electrical current density. It was found that insulating the gap between the semiconductors legs or operating TEG in vacuum helps in improving the device efficiency. Morega [18] explored numerical model of a single TEG on the basis of Onsagers principle that relates gradient to flux for temperature and electric potential. The equations were solved by using the commercial finite element software COMSOL Metaphysics. One-dimensional numerical model using iteratively finite difference algorithm was introduced by Fateh et al. [19]. Heat transfer and temperature distribution were accounted for the governing equations. Two modules were evaluated to validate their numerical results. The validation showed a good agreement of the maximum power harvested over the thicker module.

The coupling between the thermodynamics and heat transfer was accounted for by Meng et al. [20]. The values of the properties were those at the average temperature. For steady-state, solution of temperature profile of p-type and n-type semiconductors was used to estimate the power harvested. Ming et al. [21] introduced TEG with eight couples. Performance prediction was performed by a three-dimensional model that uses the finite element method. To enhance the power output, they constructed a single leg that was built on segments of different materials. Zhou [22] built a two-dimensional heat transfer numerical model for vehicle exhaust application. The cooling

process was performed by using an engine cooling system through tubes. Their results showed that increasing the exhaust flow rate enhances the power output. A TEG one-dimensional model based on heat transfer differential equation operating in high temperature environment was developed using SPICE which integrated a circuit simulation program [23]. The study showed time stabilization of voltage output over a range of load resistances and open circuit values under steady-state. Kim [24] investigated the performance of a thermoelectric energy recovery module by testing a model vehicle inside a portable wind tunnel. The optimum resistance which generates high levels of power was found to be near the internal resistance of TEG used.

Baranowski et al. [25] developed an effective thermal conductivity parameter which involved using Fourier and thermoelectric heat transport. The parameter was independence from the TEG's operating condition. This term helped to estimate TEG's maximum power output. Lee et al. [26] defined effective values for three main material properties. The effective material properties for Seebeck coefficient, electrical resistance and thermal conductivity were written in terms of three maximum parameters of temperature gradient, electrical current and cooling power. The results showed good agreement with performance data for four commercial thermoelectric cooler modules. Kim [27] investigated the Seebeck coefficient and the TEG's internal resistance experimentally from voltage-current curves. It was helpful to express the temperature gradient in term of load current which can predict the TEG's performance. Hsu et al. [28] evaluated an effective Seebeck coefficient experimentally by applying two different clamping forces to increase the contact resistance of the TEG. Therefore, it related power estimation to characteristics behavior under operating conditions. Chien et al. [29] evaluated temperature-dependent effective properties for

the TEG, which was validated experimentally using a commercial TEG module. The goal was to predict the effective performance for single or several TEG modules at any operating condition.

Morega et al. [18] investigated geometry optimization of the TEG by integrating Maxwell's equations for electromagnetic field and heat transfer law. It was found that efficiency for optimum TEG depended on the aspect ratio, internal resistance of TEG and the load resistance. Su et al. [30] improved TEG power gained by optimizing the amount of heat applied on TEG's hot side that was attached to automotive exhaust. TEG efficiency was improved by reaching a high surface temperature and uniforming temperature distribution. Jang et al. [31] investigated the energy harvesting from TEG modules attached to a gas chimney. The TEG were cooled by water. The spacing between modules was optimized to generate more heat recovery energy using TEG modules. He et al. [32] developed a mathematical model for TEG placed on an exhaust pipe of the vehicle. The model showed the effects of the temperature difference and the exhaust gas flow rate. It was found that the maximum power generated from the TEG increased as the gas flow rate increases. Meng et al. [33] discovered the optimization in design for bismuth-telluride TEG module with a base area of 4x4 mm^2. The optimization parameters included the number of elements, leg height and base area ratio. The TEG's leg height inversely impacted the level of harvested power. A segmented thermoelectric generator was investigated by Tian et al. [34]. They were able to harvest power from an exhaust pipe of a diesel engine. For large temperature differences, the segmented model predicted a higher efficiency than traditional analytical model. Also, the maximum harvested power was reduced by increasing the TEG's leg height. Favarel et al. [35] developed a simulation model that included the heat transfer from both TEG sides. It was found that the position of TEG modules is important to

extract more heat recovery energy from automotive exhaust pipe. Moreover, distributing the TEG modules on polymer electrolyte membrane (PEM) fuel cell exhaust enhanced waste-heat recovery energy [36].

A thermoelectric generator model can be improved by accounting for the temperature-dependence of semiconductors properties. The Thomson effect is neglected if constant-properties are considered. Manufacturers might provide model or data sheet for the performance which could be usable only for their devices. Therefore, a generalized model is needed to predict power harvested from TEG over various conditions. An empirical model was developed and validated with experimental measurements by Hsu et al. [37]. Their results cover hot temperatures up to 97 ^{o}C. However, the temperature differences were below 20 ^{o}C. The empirical model showed that the Seebeck coefficient can be written as quadratic polynomial function of the temperature. Also, the internal resistance and temperature had a linear relationship. This implies that, the relationship between electrical resistivity and temperature is linear [38]. In this chapter, a simplified model is developed to predict TEGs performance. The model is based on the energy and electrical potential field equations. The model is then used to perform a sensitivity analysis for the effects of varying specific parameters on the performance of TEGs. The uncertainty analysis using numerical model accounts for temperature-dependent properties, geometric and temperature boundary conditions. We should note here that this analysis can not be performed using the analytical methods. The goal is to recognize the effects of the correlations of different input parameters on the TEG performance.

2.2 Numerical model and simulation

2.2.1 Governing equations

The developed numerical model is based on the coupling of the energy and electrical potential field equations. The energy equation is derived from the heat diffusion equation which is given by:

$$-\nabla \cdot \overrightarrow{q} + \dot{q} = C_p \frac{\partial T}{\partial t} \tag{2.1}$$

where $\overrightarrow{q}$ is the heat flux vector, $\dot{q}$ is the heat production and C_p is the specific heat capacity at constant pressure. At steady state, the left side is equal to zero and Equation (2.1) is written as:

$$-\nabla \cdot \overrightarrow{q} + \dot{q} = 0 \tag{2.2}$$

Based on the Thomson effect and Onsagers principle, the heat flux $\overrightarrow{q}$ is given by:

$$\overrightarrow{q} = \alpha T \overrightarrow{J} - k\nabla T \tag{2.3}$$

where T is the absolute temperature, α is the Seebeck coefficient, k is the thermal conductivity and $\overrightarrow{J}$ is the current density. The heat production can be defined as the dot product of the electric field and current density [39] which yields:

$$\dot{q} = \frac{J^2}{\sigma} + \overrightarrow{J} \cdot \alpha \nabla T \tag{2.4}$$

where σ is the electrical conductivity.

By substituting Equations (2.3) and (2.4) into Equation (2.2), one obtains

$$\nabla \cdot (k\nabla T) + \frac{J^2}{\sigma} - \beta \overrightarrow{J} \cdot \nabla T = 0 \tag{2.5}$$

The first term on the left side represents Fourier heat conduction. The second term represents the Joule heating, which accounts for heat generation by the electrical current. The third term represents the Thomson effect, which describes the heating of a conductor with temperature gradient, where β is the Thomson coefficient and is defined as:

$$\beta = T\frac{d\alpha}{dT} \tag{2.6}$$

Assuming that the Seebeck coefficient is independent of the temperature, Equation (2.5) is reduced to a simple differential equation that relates the generated current to the temperature gradient. On the other hand, the Thomson effect indicates that the temperature dependence of the Seebeck coefficient leads to distributed heating and cooling within the conducting medium. This distribution impacts the electric potential as such:

$$\nabla.(\sigma(\nabla\phi - \alpha\nabla T)) = 0 \tag{2.7}$$

where ϕ is the electric potential and $\alpha\nabla T$ is the Seebeck electromotive force. The electric field

$$\overrightarrow{E} = -\nabla\phi + \alpha\nabla T \tag{2.8}$$

is related to the current density vector by:

$$\overrightarrow{J} = \sigma\overrightarrow{E} \tag{2.9}$$

Therefore, the second governing equation relates the current density vector to the gradient of the electric potential and the electromotive force.

$$J = -\sigma\nabla\phi + \sigma\alpha\nabla T \tag{2.10}$$

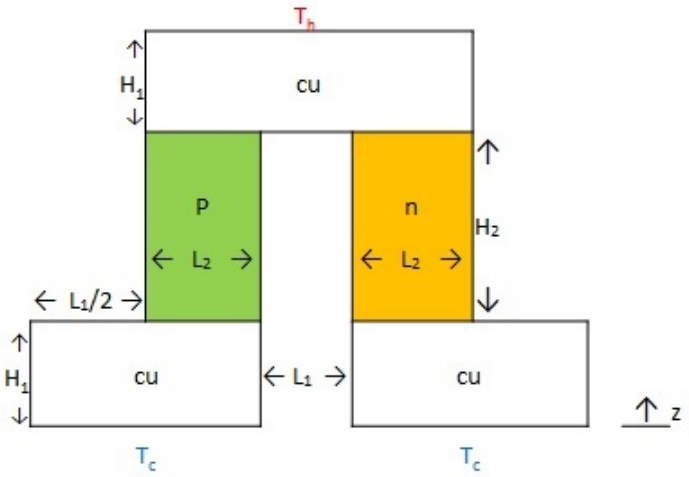

Figure 2.1: TEG single element.

Assuming no variations along the cross-section, we obtain a one-dimensional version of the governing equations. The energy equation is then written as:

$$k\sigma T'' + (k'\sigma - \beta\sigma J)T' + J^2 = 0 \tag{2.11}$$

and the second governing equation is given by:

$$\alpha\sigma T' - \sigma\phi' - J = 0 \tag{2.12}$$

where $(...)' = \frac{d}{dz}$.

As such, the current density is constant and defined as:

$$J = \frac{i}{A} \tag{2.13}$$

where i is the current for a single TEG element related to the two semiconductors and A is the cross-sectional area. As a first guess, we estimate this value to be:

$$i_0 = const. = \frac{\bar{\alpha}\Delta T}{\bar{R}_i} = \frac{\bar{\alpha}(T_h - T_c)}{\bar{\rho}\frac{H_2}{L_2^2}} \tag{2.14}$$

where the average Seebeck coefficient, $\bar{\alpha}$, is calculated at the average temperature:

$$\bar{\alpha} = \alpha_p(T_{avg}) - \alpha_n(T_{avg}) \tag{2.15}$$

and the average electrical resistivity, $\bar{\rho}$, is given by:

$$\bar{\rho} = \frac{1}{\bar{\sigma}} = \rho_p(T_{avg}) + \rho_n(T_{avg}) \tag{2.16}$$

Once we run the simulation, we iterate the obtained solution to converge towards the correct value of i.

We assume square cross-sectional areas of the semiconductors that are given by:

$$A_p = A_n = L_2^2 \tag{2.17}$$

For the interconnector, which is made out of copper. The cross-sectional area is given by:

$$A_{cu} = \left(L_2 + \frac{L_1}{2}\right)^2 \tag{2.18}$$

2.2.2 Governing equations for TEG element

We write the governing equations for the three materials that constitute a single TEG element. Each material has two governing equations for the copper and p-type and n-type semiconductors which are derived from Equations (2.11) and (2.12) as follows:

For copper, the governing equations are;

$$k_{cu}\sigma_{cu}T''_{cu}\left(k'_{cu}\sigma_{cu} - \beta_{cu}\sigma_{cu}\frac{i}{A_{cu}}\right)T'_{cu} + \left(\frac{i}{A_{cu}}\right)^2 = 0 \tag{2.19}$$

$$\alpha_{cu}\sigma_{cu}T'_{cu} - \sigma_{cu}\phi'_{cu} - \frac{i}{A_{cu}} = 0 \tag{2.20}$$

for the p-type semiconductor;

$$k_p\sigma_p T''_p\left(k'_p\sigma_p - \beta_p\sigma_p\frac{i}{A_p}\right)T'_p + \left(\frac{i}{A_p}\right)^2 = 0 \tag{2.21}$$

$$\alpha_p\sigma_p T'_p - \sigma_p\phi'_p - \frac{i}{A_p} = 0 \tag{2.22}$$

and for the n-type semiconductors;

$$k_n\sigma_n T''_n\left(k'_n\sigma_n - \beta_n\sigma_n\frac{i}{A_n}\right)T'_n + \left(\frac{i}{A_n}\right)^2 = 0 \tag{2.23}$$

$$\alpha_n\sigma_n T'_n - \sigma_n\phi'_n - \frac{i}{A_n} = 0 \tag{2.24}$$

Bismuth-telluride is the most commonly used semiconductor material in manufacturing thermoelectric generators. The properties of this material are a function of the temperature, which is turn is a function of z. These properties are determined using the following equations:

$$\alpha_q(z) = a_1T_q^2(z) + a_2T_q(z) + a_3 \tag{2.25}$$

$$k_q(z) = b_1T_q^2(z) + b_2T_q(z) + b_3 \tag{2.26}$$

$$\rho_q(z) = \frac{1}{\sigma_q(z)} = c_1T_q^2(z) + c_2T_q(z) + c_3 \tag{2.27}$$

Material	p-type	n-type	Copper
$a_1 10^{-9}(V/K^3)$	-2.541	1.246	-
$a_2 10^{-6}(V/K^2)$	2.123	-1.005	-
$a_3 10^{-3}(V/K)$	-0.2345	0.02128	0.0065
$b_1 10^{-6}(\frac{W}{mK^3})$	47.68	6.4681	-
$b_2 10^{-3}(\frac{W}{mK^2})$	-35.888	-5.807	-
$b_3(\frac{W}{mK})$	7.914	2.323	386
$c_1 10^{-10}(\frac{\Omega m}{K^2})$	-0.453	-1.416	-
$c_2 10^{-8}(\frac{\Omega m}{K})$	7.359	15.935	-
$c_3 10^{-6}(\Omega m)$	-7.437	-26.473	0.0017

Table 2.1: Materials constants.

Table (2.1) gives values of the constants in Equations (2.25)-(2.27).

Next, we solve the governing Equations (2.19)-(2.24) in the range from z= 0 to z=$2H_1 + H_2$. The first two boundary conditions are those of the temperature on both end sides, i.e.

$$T_{cu}(0) = T_c \tag{2.28}$$

$$T_{cu}(2H_1 + H_2) = T_h \tag{2.29}$$

Three boundary conditions are set at the temperature interferences between the copper and the two

semiconductors, i.e.

$$T_{cu}(H_1) = T_p(H_1) \tag{2.30}$$

$$T_{cu}(H_1) = T_n(H_1) \tag{2.31}$$

$$T_{cu}(H_1 + H_2) = T_p(H_1 + H_2) \tag{2.32}$$

$$T_{cu}(H_1 + H_2) = T_n(H_1 + H_2) \tag{2.33}$$

and the electrical potential at the bottom copper plate is also set to zero.

$$\phi_{cu}(0) = 0 \tag{2.34}$$

Two boundary conditions are also set at the interferences of the electrical potential, i.e.

$$\phi_{cu}(H_1) = \phi_p(H_1) \tag{2.35}$$

$$\phi_{cu}(H_1) = \phi_n(H_1) \tag{2.36}$$

2.2.3 Model output

By solving Equations (2.19)-(2.24) with the boundary conditions stated above (2.28)-(2.36), the voltage produced from a single TEG element is determined as:

$$V_{oc} = \phi_p(H_1 + H_2) - \phi_p(H_1) + \phi_n(H_1 + H_2) - \phi_n(H_1) \tag{2.37}$$

Using a single element circuit such as the one shown in Figure (2.2), the power output is given by:

$$P = I^2 R_L \tag{2.38}$$

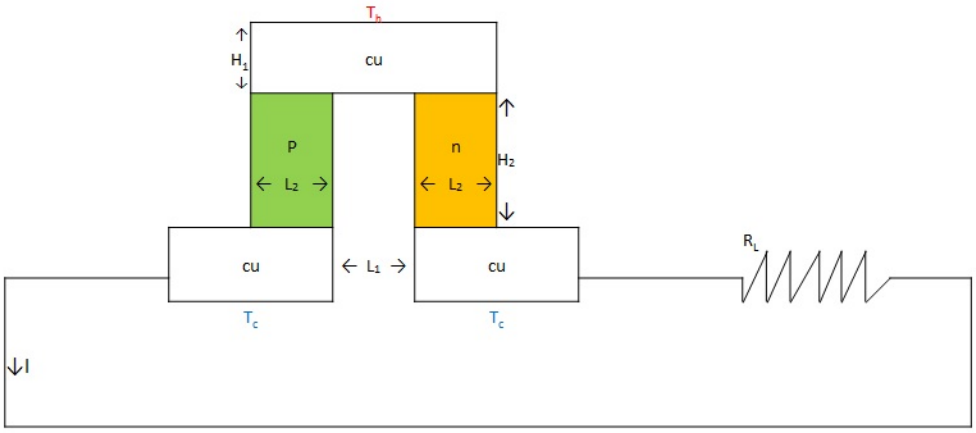

Figure 2.2: Single element electrical circuit.

For a multi-element TEG as shown in Figure (2.3), the elements are connected electrically in series. Therefore, the voltage generated and internal resistance can be calculated by multiplying the number of element with the power value of a single element.

$$P_{N_e} = \left(\frac{N_e V_{oc}}{(N_e R_i + R_L)} \right)^2 R_L \tag{2.39}$$

where N_e is number of element and R_i is the internal resistance of the semiconductors. The p-type and n-type internal resistance are given by:

$$R_p(z) = \rho_p(z)\frac{H_2}{A_p} \tag{2.40}$$

$$R_n(z) = \rho_n(z)\frac{H_2}{A_n} \tag{2.41}$$

The internal resistance of one TEG unit is then given by:

$$R_i = R_p\left(z = H_1 + \frac{H_2}{2}\right) + R_n\left(z = H_1 + \frac{H_2}{2}\right) \tag{2.42}$$

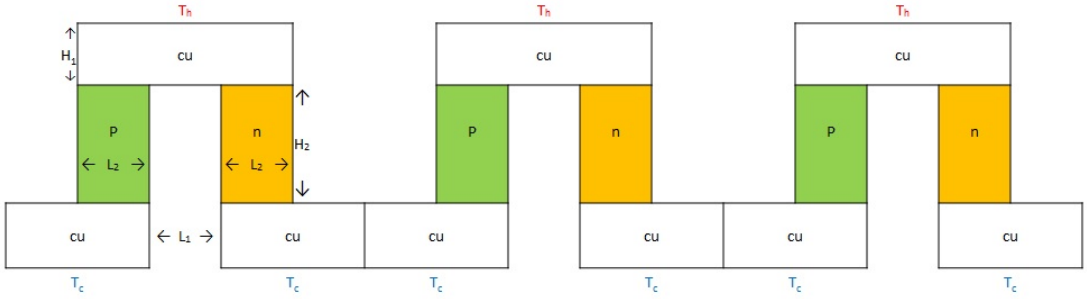

Figure 2.3: Multi-element TEG.

2.2.4 Iteration procedure

We started with the same initial guess of the current for different values of ΔT using Equation (2.14). The iterated current value is given by:

$$i_{j+1} = \frac{\alpha_j(T_h - T_c)}{\rho_j \frac{H_2}{L_2^2}} \tag{2.43}$$

where j is the iteration, j=1,2,..,10. The iterated Seebeck coefficient, α_j, is calculated at the middle of the TEG's element:

$$\alpha_j = \alpha_p\left(z = H_1 + \frac{H_2}{2}\right) - \alpha_n\left(z = H_1 + \frac{H_2}{2}\right) \tag{2.44}$$

and the iterated electrical resistivity at the middle of the TEG's element, ρ_j, is given by:

$$\rho_j = \rho_p\left(z = H_1 + \frac{H_2}{2}\right) + \rho_n\left(z = H_1 + \frac{H_2}{2}\right) \tag{2.45}$$

We observed that after few iterations (less than three), the solution converged to a specific value for each case as shown in Figure (2.4). By comparing the convergence values to the initial guess in Equation (2.14), we concluded that the initial guess is a good approximation as shown in Table (2.2). So in the rest of this work, we will use Equation (2.14) to determine the current value.

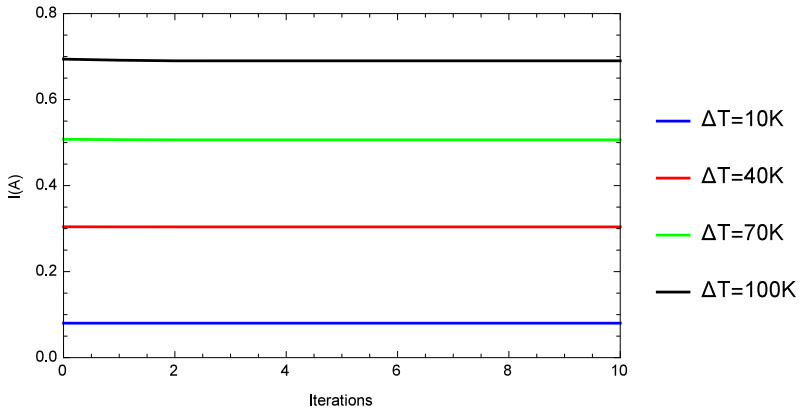

Figure 2.4: Variation of the current values versus iterations at $T_c = 300K$.

ΔT (K)	$i_{coveraged}$ (A)	$i_{initial}$ (A)
10	0.0801	0.0801
40	0.3040	0.3043
70	0.5064	0.5078
100	0.6902	0.6941

Table 2.2: Comparison between converged and initial guess of the current values.

2.3 Constant properties model

The constant properties model is a simplified model that is based on the average temperature between two junctions. The generated voltage is equal to the product of the Seebeck coefficient and the temperature difference

$$\bar{V_{oc}} = N_e \bar{\alpha} \Delta T \tag{2.46}$$

The internal resistance is given by

$$\bar{R} = N_e \bar{\rho} \frac{H_2}{L_2^2} \tag{2.47}$$

The power output from the multi-element TEG is then calculated as:

$$\bar{P} = \left(\frac{\bar{V_{oc}}}{\bar{R} + R_L} \right)^2 R_L \tag{2.48}$$

2.4 Model validation

Model validation is performed through the experimental setup shown in Figure (2.5). The heating is applied by electrical hot plate. The hot temperature was measured on an aluminum plate placed between the heating source and the TEG. On the cooling side, we used a cold plate with a single pass loop whereby the water pushes through the copper tubes to decrease the aluminum plate temperature. The designed experiment performs as an open system. To ensure a continuous fluid flow, a gear pump (B& D Pumps Inc., UGP-3000) was used to pump water inside the tube. Temperature measurements were performed on the hot and cold sides using two K-type thermocouples purchased from Omega Engineering, Inc..

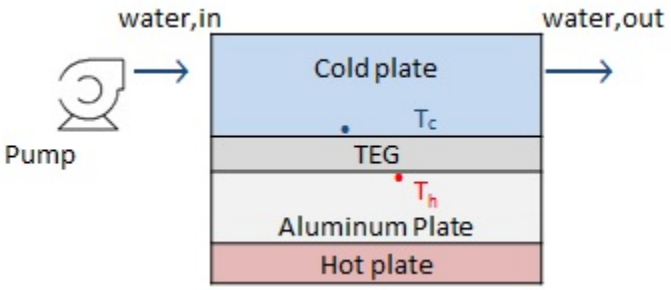

Figure 2.5: Diagram of the experimental setup.

Three different TEG modules were used in performing the experiments. Table (2.3) shows the specifications of each of these modules. A hot plate was introduced in the experimental setup and it is treated as the heat source. To reach steady-state conditions, the cooling source and hot plate were turned on and allowed enough time to obtain constant temperatures. The open circuit voltage was measured for eight temperature differences. For each temperature difference, a load resistance was connected to close the loop as shown in Figure (2.6). Load voltages were measured for fourteen

different load resistances. The generated power was calculated by applying the following equation:

$$P_{exp} = \frac{V_L^2}{R_L} \tag{2.49}$$

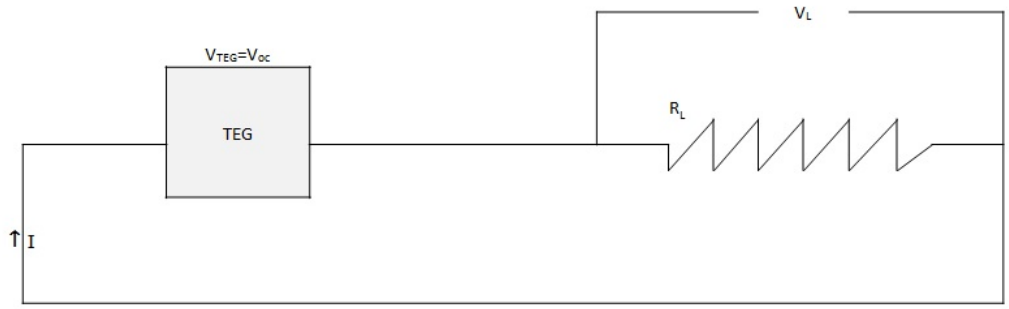

Figure 2.6: The electrical circuit of the performed experiments.

Parameter	Laird CP10,127,05	Laird CP10,127,08	Marlow TG12-2.5-01L
$Length(mm)$	30	30	30
$Width(mm)$	30	30	30
$Thickness(mm)$	3.2	4	3.94
N_e	127	127	127
$H_1(mm)$	0.1397	0.1397	0.1397
$H_2(mm)$	1.27	2.032	2.032
$L_1(mm)$	0.7874	0.7874	0.7874
$L_2(mm)$	0.762	0.762	0.762

Table 2.3: TEG modules parameters.

2.5 Results and Discussion

2.5.1 Power generated

Figures (2.7)-(2.9) show the power generated from each of the three TEG modules as a function of the load resistance. In each plot, three sets of the data are presented. The first is obtained from the measurements. The second one is obtained by using average temperature predictions. The third one is obtained from the numerical model. In general, the prediction from the analytical representation based on an average temperature is larger than that of the numerical model. This difference becomes more pronounced as the temperature difference is increased. Furthermore, the numerical model overpredicts the power generated for both the Laird CP10,127,05 and Marlow TG12-2.5-0.1L. On the other hand, better prediction is obtained for the numerical, especially at high ΔT for the Larid CP10,127,08. This may be due to the fact that the one-dimensional approximation is more accurate as the height of the element is increased.

2.5.2 Internal resistance analysis

Considering Figures (2.6)-(2.8), we note that the power peaks are not obtained for the same values of load resistance. Analytically, the internal resistance of the TEG module can be calculated from the constant properties model.

$$\bar{R}_i = \bar{R} \tag{2.50}$$

The predictions of the maximum output power for both numerical and analytical are obtained when

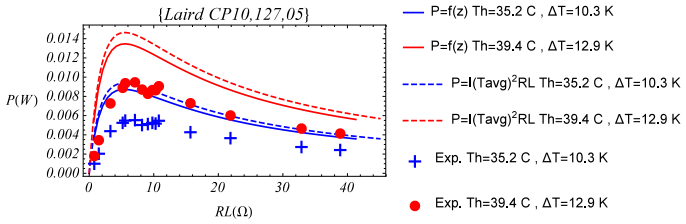

(a) $T_h = 35.2^oC, \Delta T = 10.3^oC, and T_h = 39.4^oC, \Delta T = 12.9^oC$.

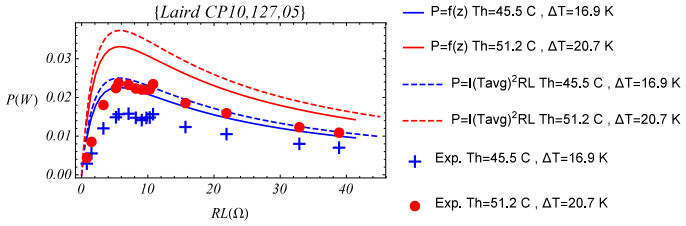

(b) $T_h = 45.5^oC, \Delta T = 16.9^oC, and T_h = 51.2^oC, \Delta T = 20.7^oC$.

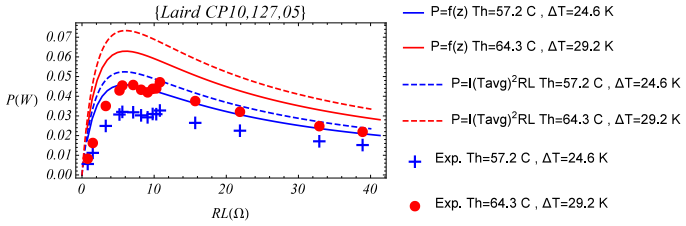

(c) $T_h = 57.2^oC, \Delta T = 24.6^oC, and T_h = 64.3^oC, \Delta T = 29.2^oC$.

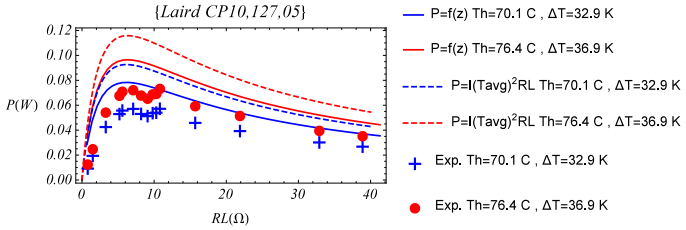

(d) $T_h = 70.1^oC, \Delta T = 32.9^oC, and T_h = 76.4^oC, \Delta T = 36.9^oC$.

Figure 2.7: Power generated versus load resistance for Laird CP10,127,05.

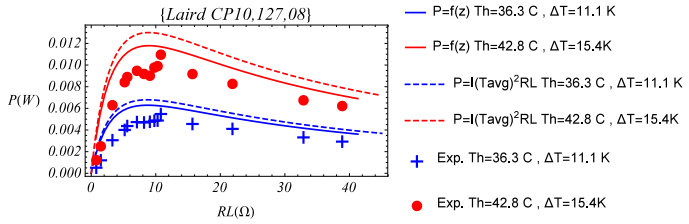

(a) $T_h = 36.3^oC, \Delta T = 11.1^oC, and T_h = 42.8^oC, \Delta T = 15.4^oC.$

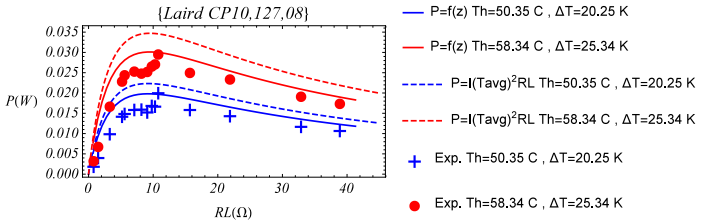

(b) $T_h = 50.4^oC, \Delta T = 20.3^oC, and T_h = 58.3^oC, \Delta T = 25.3^oC.$

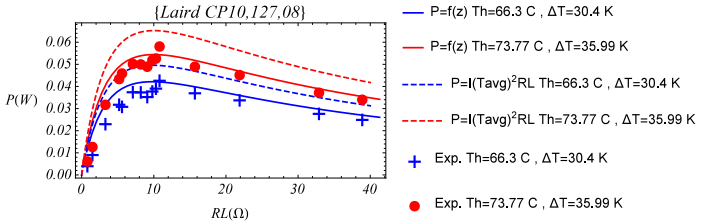

(c) $T_h = 66.3^oC, \Delta T = 30.4^oC, and T_h = 73.8^oC, \Delta T = 36^oC.$

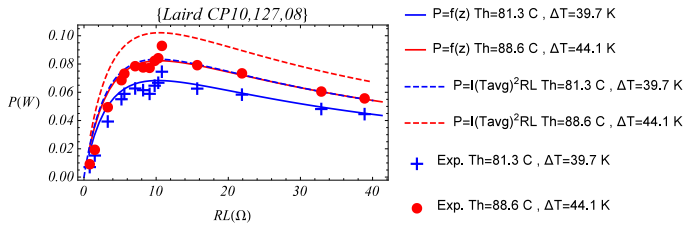

(d) $T_h = 81.3^oC, \Delta T = 39.7^oC, and T_h = 88.6^oC, \Delta T = 44.1^oC.$

Figure 2.8: Power generated versus load resistance for Laird CP10,127,08.

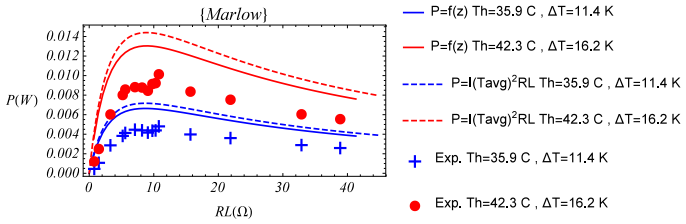

(a) $T_h = 35.9^oC, \Delta T = 11.4^oC, and T_h = 42.3^oC, \Delta T = 16.2^oC.$

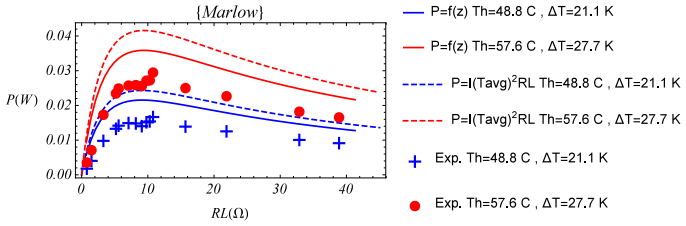

(b) $T_h = 48.8^oC, \Delta T = 21.1^oC, and T_h = 57.6^oC, \Delta T = 27.7^oC.$

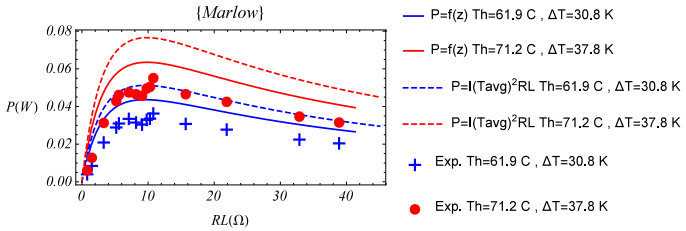

(c) $T_h = 61.9^oC, \Delta T = 30.8^oC, and T_h = 71.2^oC, \Delta T = 37.8^oC.$

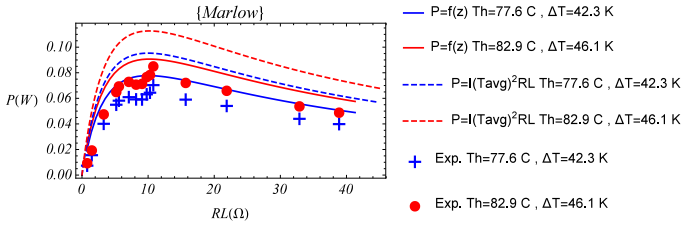

(d) $T_h = 77.6^oC, \Delta T = 42.3^oC, and T_h = 82.9^oC, \Delta T = 46.1^oC.$

Figure 2.9: Power generated versus load resistance for Marlow TG12-2.5-01L.

the load resistance is equal to the internal resistance.

$$R_i = \bar{R}_i \tag{2.51}$$

Experimentally, one could determine the internal resistance from the relation:

$$V_L = V_{oc} - I_L R_{exp} \tag{2.52}$$

where V_L is the load resistance, V_{oc} is the open circuit voltage and I_L is the current. From this relation, the internal resistance can be determined from the slope of the voltage when plotted against the current.

$$R_{exp} = -\frac{dV_L}{dI_L} \tag{2.53}$$

Figure (2.10) shows the internal resistance as a function of the temperature difference ΔT for the three modules. The results show a slight increase as ΔT is increased, which is expected because the resistance increases slightly with the temperature. Figure (2.11) shows the ratio of the experimental internal resistance to its analytical counterpart.

$$\theta = \frac{R_{exp}}{R_i} \tag{2.54}$$

The results also show the values to range between 1.05 and 1.15, thus providing a higher ratio for the Laird CP10,127,05 and Laird CP10,127,08 than that of Marlow TG12-2.5-01L. This ratio deceases slightly as ΔT is increased. We should note here that the T_c in all experiments was more or less constant for all TEG modules. The decrease in the ratio is associated with the increase of the hot temperature T_h.

Next, we compare the experimental maximum power generated for the three different modules. Because all three modules have the same surface area, we can relate the maximum power harvested

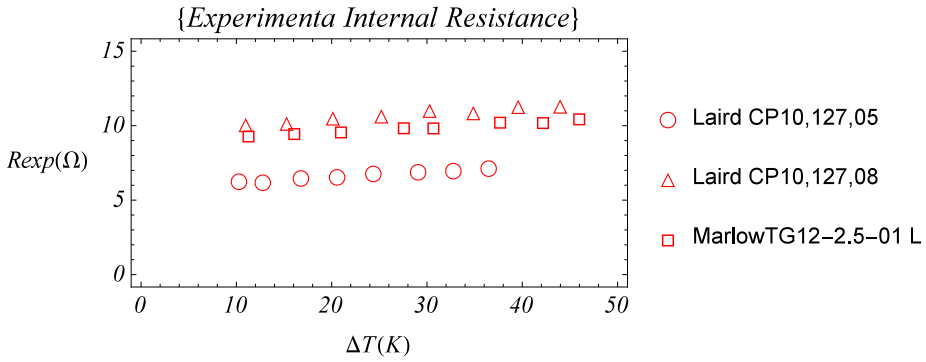

Figure 2.10: The experimental internal resistance for the three TEG modules.

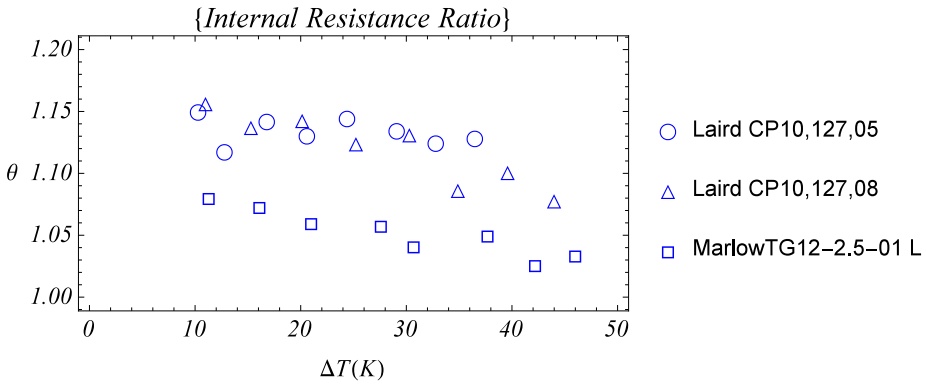

Figure 2.11: The internal resistance ratio for the three TEG modules.

with the power density for each module. It is depicted in Figure (2.12) that the Laird CP,127,05 harvested more power than the other devices.

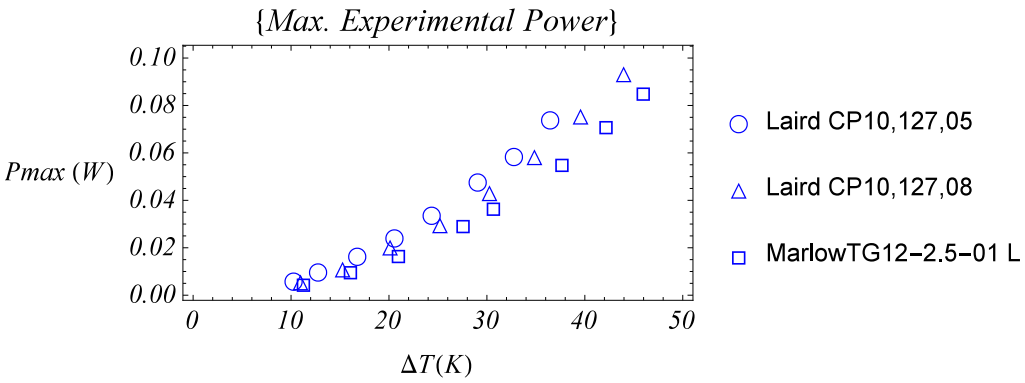

Figure 2.12: The experimental maximum power gained for the three TEG modules.

2.6 Comparison with manufacturing model

2.6.1 Hi-Z model

Hi-Z Technology, Inc. [40] developed a performance model of their products that provides the coefficient of the thermoelectric generator as a function of the average temperature between the two sides. As shown in Figures (2.13)-(2.15), the Seebeck coefficient, electrical resistivity and thermal conductivity are approximated by quartic functions of the average temperature. In this work, we chose two Hi-Z modules, HZ-2 and HZ-14, and compared their performance based on these coefficients with our numerical predictions. Table (2.4) shows the parameters of the chosen Hi-Z thermoelectric generators.

The open circuit voltage is calculated as follows:

$$V_{HiZ} = 0.89 N_e [\alpha_p(f(T_{avg}) - \alpha_n(f(T_{avg})] \tag{2.55}$$

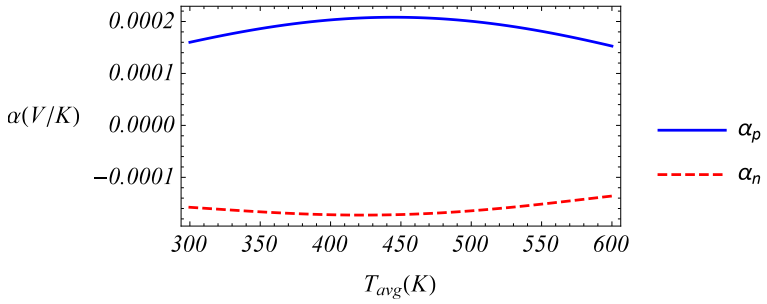

Figure 2.13: The Seebeck coefficient for Hi-Z model.

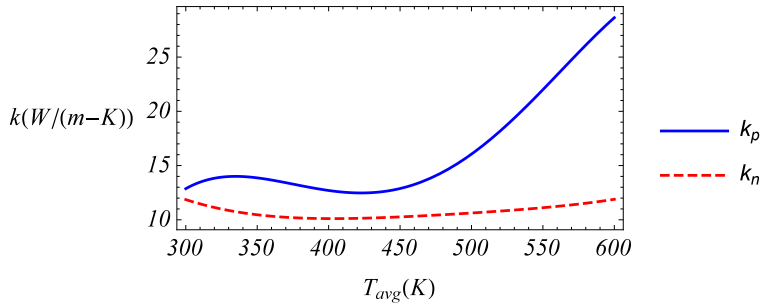

Figure 2.14: The thermal conductivity for Hi-Z model.

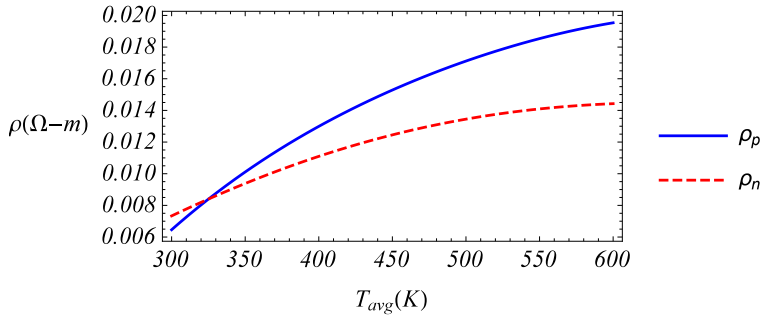

Figure 2.15: The electrical resistivity for Hi-Z model.

The internal resistance as defined by the manufacture is given by:

$$R_{HiZ} = \frac{1.25}{1000} N_e \frac{H_2}{L_2^2} [\rho_p(f(T_{avg}) - \rho_n(f(T_{avg})] \tag{2.56}$$

Parameter	HZ-2	HZ-14
$Length(cm)$	2.9	6.27
$Width(cm)$	2.9	6.27
$Thickness(cm)$	0.508	0.508
$H_1(cm)$	0.2	0.15
$H_2(cm)$	0.287	0.16
$L_1(cm)$	0.05	0.18
$L_2(cm)$	0.154	0.383
N_e	97	49

Table 2.4: Hi-Z specifications for the two modules.

The power output based on the Hi-Z model is expressed as:

$$P_{HiZ} = \left[\frac{V_{HiZ}}{R_{HiZ} + R_L}\right]^2 R_L \tag{2.57}$$

2.6.2 Results and Discussion

The results presented in Figures (2.16) and (2.17) show that the analytical model overpredicts the harvested power than that of the numerical and manufacture model. However, HZ-2 shows a very good agreement with the numerical prediction in the high and low temperature difference conditions as shown in Figure (2.16). For the HZ-14 module, the numerical model shows a large separation from the manufacturer's data as the temperature difference increased as shown in Figure

(2.17). The difference in prediction between the three models become smaller as the load resistance increases. Due to the different semiconductors geometry for both modules, the optimum resistance which maintains maximum power is not the same for both modules.

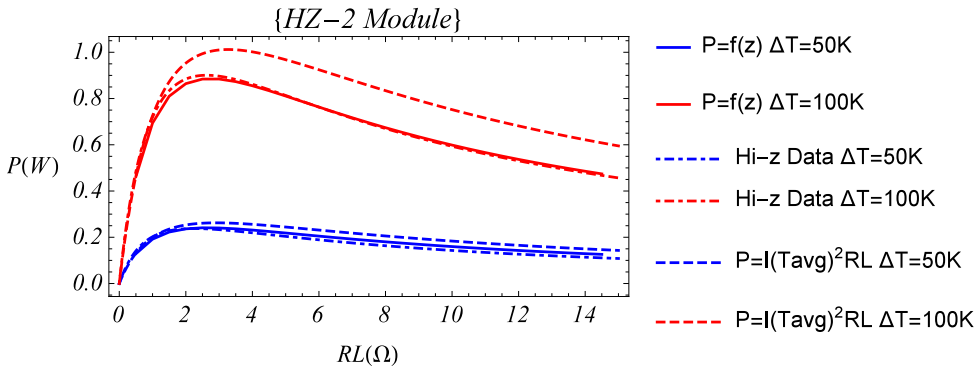

Figure 2.16: Power versus load resistance for HZ-2 module.

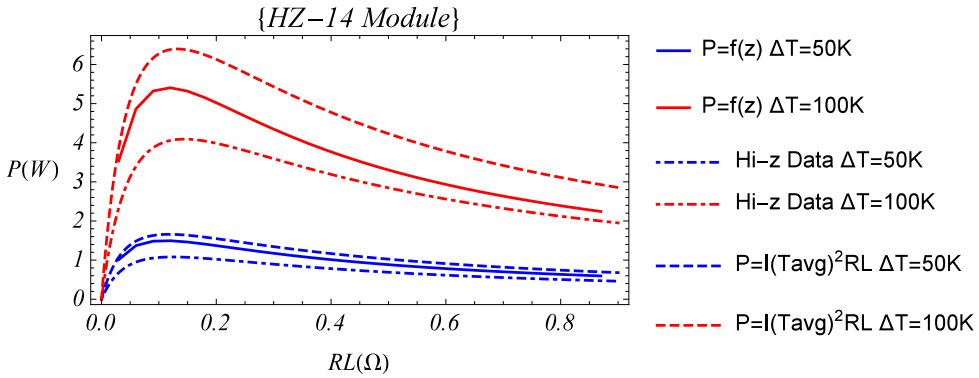

Figure 2.17: Power versus load resistance for HZ-14 module.

2.7 Sensitivity analysis

In Section 2.5, the performance of the three different TEG modules were validated experimentally with certain geometric specifications and parameters for the semiconductor material. Next,

we perform sensitivity analysis to determine input parameters such as TEG leg dimensions, material properties and temperature boundary conditions affect on harvested voltage and power. The analytical prediction limits or neglects the effects of specific variations in thermal conductivity, electrical resistivity, Thomson effect and TEG's element dimensions. In particular, the TEG open circuit voltage is only a function of temperature gradient and the Seebeck coefficient. Three advantages for using uncertainty analysis which can have an impact on the TEG performance. First, uncertainty analysis of the effects of the material properties could help in improving or designing new material. Second, geometry sensitivity-analysis can help in the geometric design. Finally, variations in the TEG boundary temperatures are important to estimate the power gained.

2.7.1 Summary of the numerical simulation

The numerical model divides the TEG element into three parts. The energy and electrical potential field governing equations are derived for each part. The energy equation for semiconductors and copper materials are given in Equations (2.19), (2.21) and (2.23), respectively. The electric potential field for each material are given in Equations (2.20), (2.22) and (2.24). The simplified numerical model solves the governing equations with nine boundary conditions based on temperature interference between the semiconductors and copper as shown in Equations (2.28)-(2.36). The surface temperatures of the TEG are set as boundary conditions. The model outputs the open circuit voltage, Equation (2.37). For a multi-element modules the output voltage is defined by:

$$V_{N_e} = N_e V_{oc} \tag{2.58}$$

The maximum power output from TEG occurs when the internal resistance equals the load resistance, which yields:

$$P_{max} = \frac{(N_e V_{oc})^2}{4N_e R_i} = \frac{N_e (V_{oc})^2}{4R_i} \tag{2.59}$$

The mean values of the geometric parameters used to determine the uncertainty are presented in Table (2.5). Table (2.1) provided the property constants for each material used in Equations (2.25)-(2.27).

Parameter	Mean
$H_1(mm)$	0.1397
$H_2(mm)$	1.27
$L_1(mm)$	0.7874
$L_2(mm)$	0.762
N_e	127

Table 2.5: Mean geometric parameters of TEG.

2.7.2 Material properties

The variation of each property, ε, ranged from -40 % to 40 % of the mean value. We recognize here that these variations are very large, but we opted to use them to see clearly the effects of varying these parameters. Now, we write properties as function of height, z and variation, ε.

From Equation (2.25), the Seebeck coefficient is given by:

$$\alpha_q(z,\varepsilon) = \alpha_q(z) + \varepsilon\alpha_q(z) \tag{2.60}$$

We rewrite the thermal conductivity in Equation (2.26) as:

$$k_q(z,\varepsilon) = k_q(z) + \varepsilon k_q(z) \tag{2.61}$$

From Equation (2.27), the electrical resistivity as function of variation (ε) is also written as:

$$\rho_q(z,\varepsilon) = \frac{1}{\sigma_q(z,\varepsilon)} = \rho_q(z) + \varepsilon\rho_q(z) \tag{2.62}$$

From Equation (2.6), the Thomson coefficient is given by:

$$\beta_q(z,\varepsilon) = \beta_q(z) + \varepsilon\beta_q(z) \tag{2.63}$$

Next, we solve for varying properties while maintaining other properties constant (ε =0). Using the geometric parameters listed in Table (2.5), the voltage output is calculated using Equation (2.58) as function of ε:

$$V_{N_e}(\varepsilon) = N_e V_{oc}(\varepsilon) \tag{2.64}$$

Figure (2.18(a-c)) shows the relationships between voltage gained and variations in each properties for three different temperature boundary conditions. The Seebeck coefficient for p-type semiconductor decreases when the difference increases. However, the n-type semiconductor's Seebeck coefficient increases when this difference is increased. Both electrical conductivity for p-type and n-type decrease as the difference is increased. For the two semiconductors, variations

in the Thomson coefficient and thermal conductivity show no effect on the voltage output. From Figure (2.18(a-c)) the difference between electrical conductivity for p-type and n-type becomes smaller as temperature gradient increases. The linear relationship between voltage and Seebeck coefficient and the non-linear relationship between voltage and electrical conductivity is explicit in Figure(2.18).

2.7.3 TEGs geometry

Analytical method does not account for geometry parameters to estimate TEGs open circuit voltage. As shown in Equation (2.46), the analytical method predicts the performance based on the Seebeck coefficient calculated at average temperature of both sides of TEGs. Numerically, the current i in Equation (2.14) is affected by the TEGs leg height, H_2, and length, L_2. Figure (2.19) shows the comparison between the analytical and numerical methods as the leg height is increased. The figure shows that the voltage has a constant limit as the height is increased.

The aspect ratio of TEGs is the ratio between leg height and length and is written as:

$$AR = \frac{H_2}{L_2} \tag{2.65}$$

Now, the maximum power can be obtained numerically over a range of aspect ratios and length. Figure (2.20) shows that the level of power generated become more dependent on leg length and the aspect ratio as temperature difference is increased. Moreover, the generated power decreases at a higher rate when leg length is decreased or the aspect ratio increased.

In practical application, load resistance affects the power harvested from TEG. The power as func-

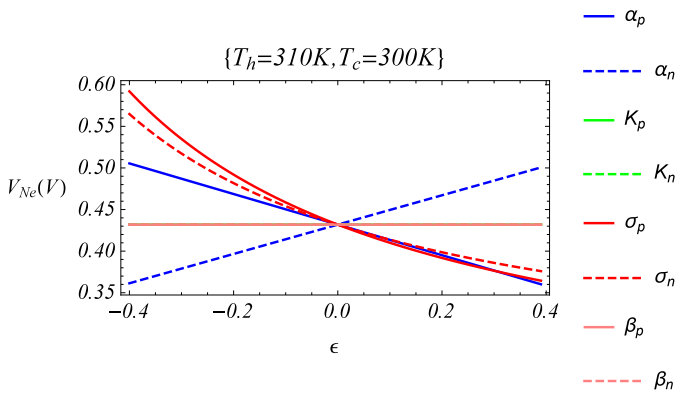

(a) $T_h = 310K and T_c = 300K$.

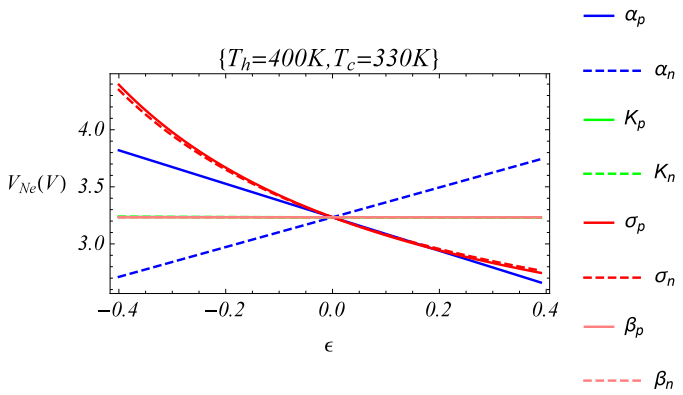

(b) $T_h = 400K and T_c = 330K$.

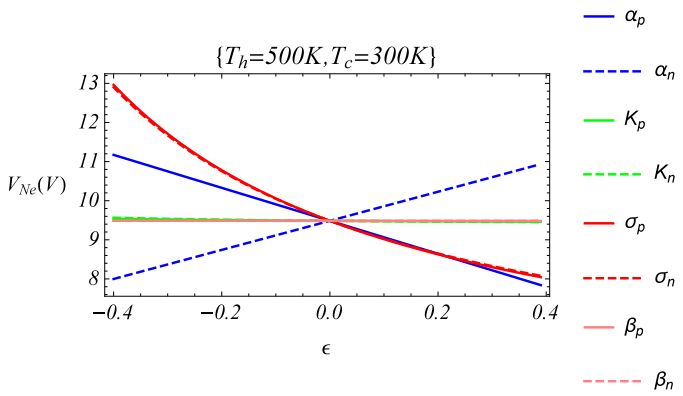

(c) $T_h = 500K and T_c = 300K$.

Figure 2.18: Output voltage versus properties variations.

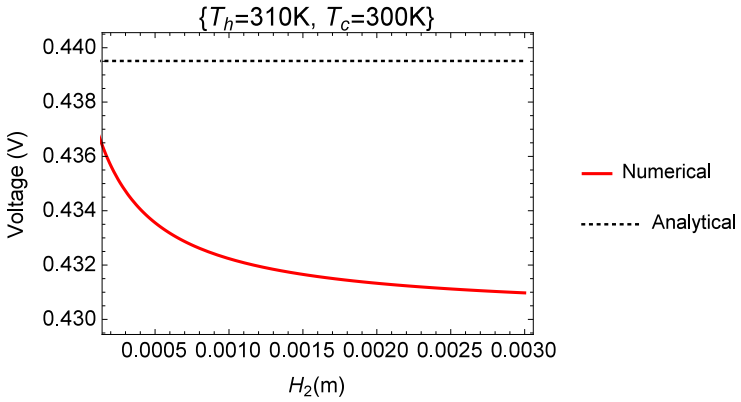

(a) $T_h = 310K and T_c = 300K$.

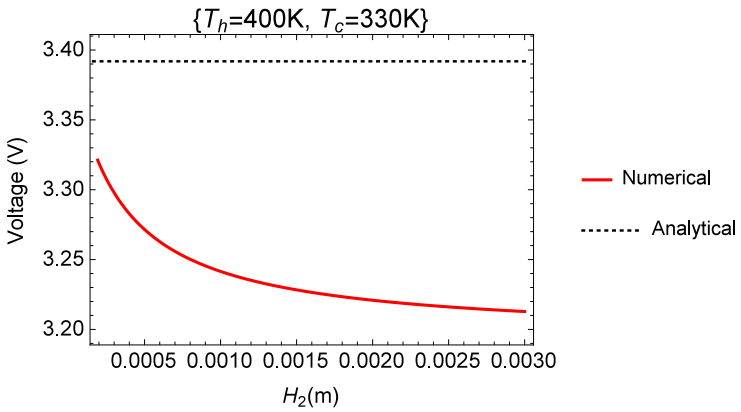

(b) $T_h = 400K and T_c = 330K$.

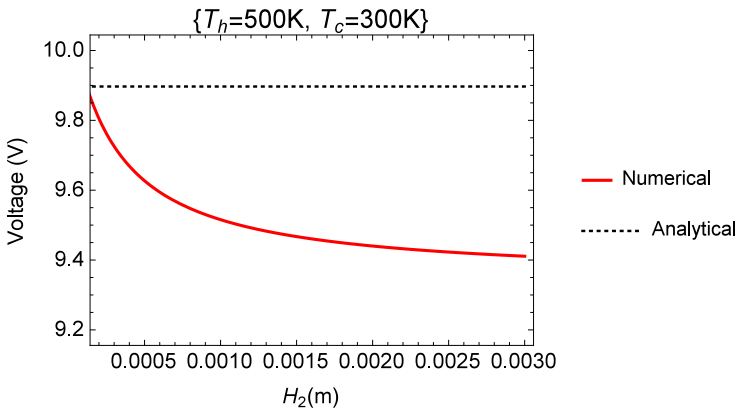

(c) $T_h = 500K and T_c = 300K$.

Figure 2.19: The numerical and analytical voltage output versus TEG leg heights.

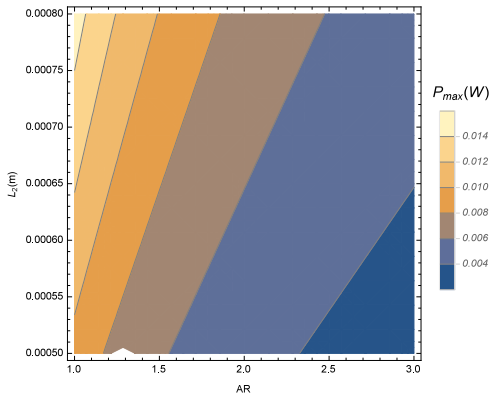

(a) $T_h = 310K and T_c = 300K$.

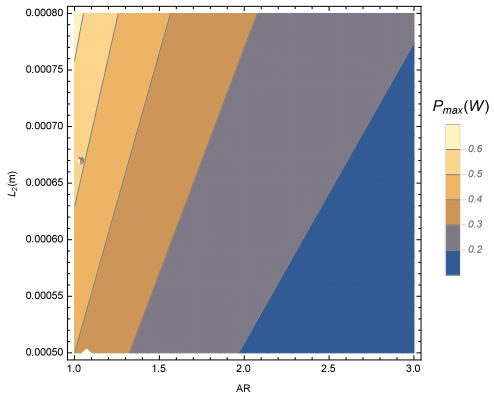

(b) $T_h = 400K and T_c = 330K$.

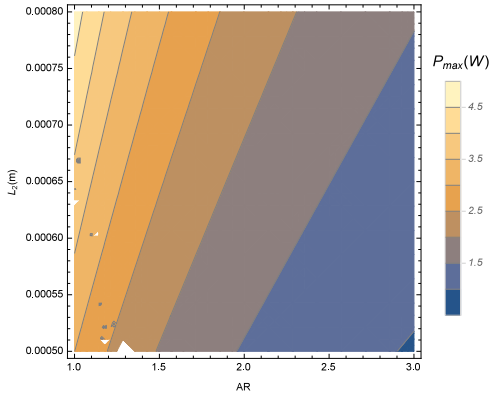

(c) $T_h = 500K and T_c = 300K$.

Figure 2.20: The range of maximum power with aspect ratio and TEG leg lengths.

tion of load resistance and leg height, H_2, or length, L_2, which are represented by the internal resistance, can be obtained using Equation (2.39). It can be solved numerically using the parameters mentioned in Table (2.5) for the copper length, L_1, height, H_1, and number of elements N_e. Figure (2.21) shows the decrease in power when the leg height, H_2, is increased. Moreover, the optimum load resistance which corresponds to maximum power decreases with increasing the leg height for specific temperature differences. In general, the power harvested increases as the temperature difference is increased. It is observed that the power increases for larger leg length TEGs. Due to change in TEGs internal resistance, the optimum load resistance shows higher value as leg length increased as shown in Figure (2.22).

2.7.4 Temperature variations

The temperature of the top and bottom surfaces of TEGs are set as boundary conditions for the numerical model. From Equation (2.28) and (2.29), the geometric parameters are used to predict the harvested power. Also, the properties constants in Table (2.1) are used. The internal resistance can be obtained from Equation (2.42). Contour plots for TEGs open circuit voltage, internal resistance and maximum power were numerically solved with varying the boundary condition temperatures. Regardless of the temperature value, the open circuit voltage for the TEGs increases when temperature gradient is increased as shown in Figure (2.23). For all temperature differences, the internal resistance increases as the average temperature is increased as shown in Figure (2.24). Figure (2.25) shows temperature gradient above 75 K has a significant increase in the maximum power harvested.

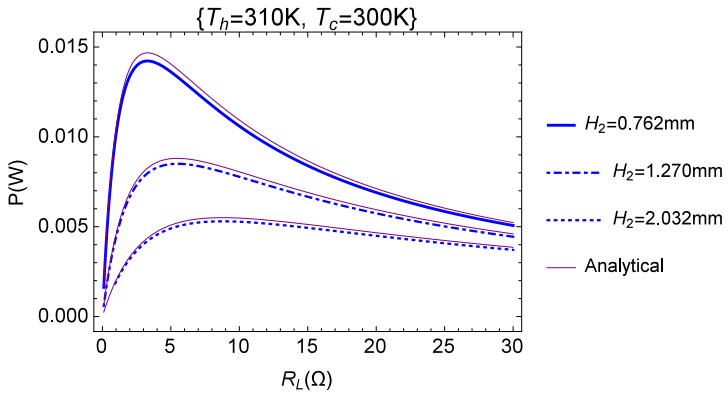

(a) $T_h = 310K and T_c = 300K$.

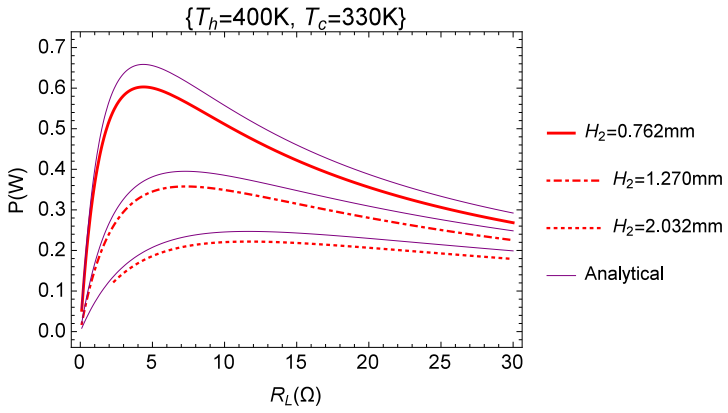

(b) $T_h = 400K and T_c = 330K$.

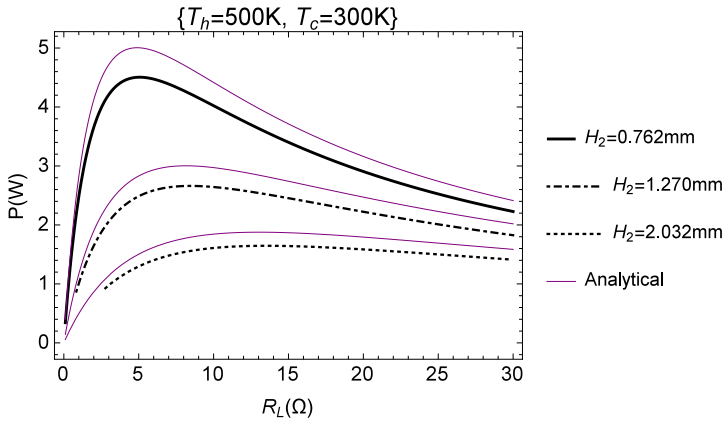

(c) $T_h = 500K and T_c = 300K$.

Figure 2.21: The power harvested versus load resistance for different leg heights.

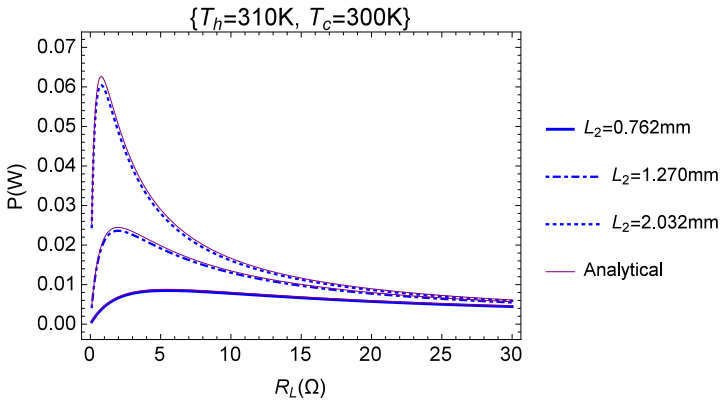

(a) $T_h = 310K and T_c = 300K$.

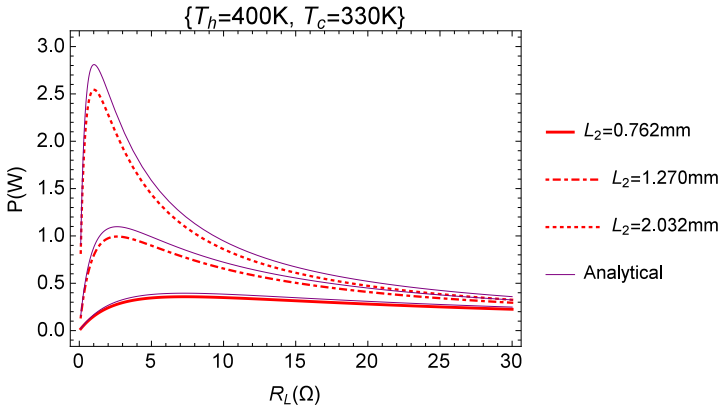

(b) $T_h = 400K and T_c = 330K$.

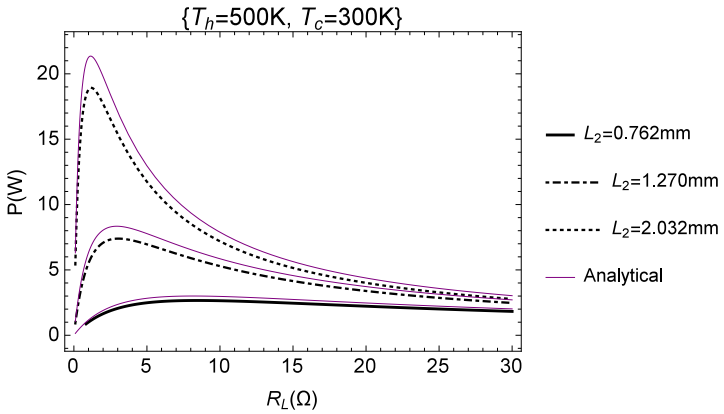

(c) $T_h = 500K and T_c = 300K$.

Figure 2.22: The power harvested versus load resistance for different leg lengths.

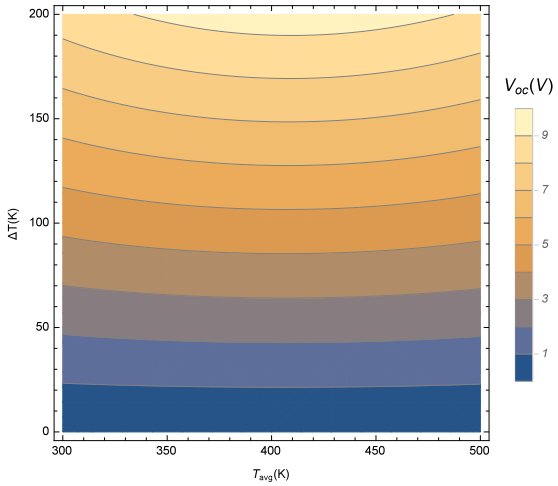

Figure 2.23: The range of TEG voltage output as function of the average temperature and temperature difference.

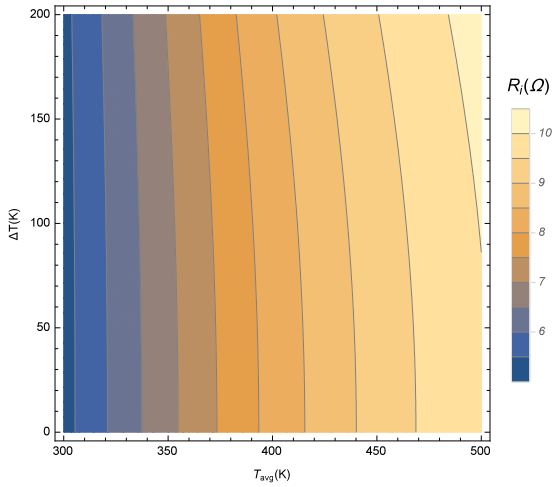

Figure 2.24: The range of TEG internal resistance as function of the average temperature and temperature difference.

2.8 Conclusions

A simplified one-dimensional model was developed to predict the performance of thermoelectric generators. Because one of the boundary conditions was unknown, an iteration procedure based on

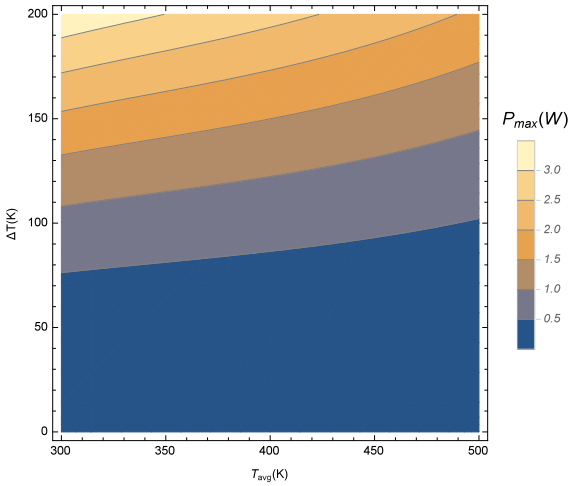

Figure 2.25: The range of TEG maximum power as function of the average temperature and temperature difference.

an initial guess of the current was suggested. The results showed the initial guess that is based on averaged quantities is a good guess and convergence takes place after three iterations. Model validation was performed by comparing predicted values of the harvested power with values measured experimentally. Three different commercial thermoelectric generators were used in the experiments. These are the Laird CP10,127,05, Laird CP10,127,08 and Marlow TG12-2.5-01L modules. The results showed that the proposed model predicted the measured values from the Laird CP10,127,08 accurately. The results also show that the accuracy of one-dimensional assumption model increases as the TEG's leg height is increased. The results also show that the model's accuracy increases as the temperature difference is increased. A comparison of the internal resistance showed that the numerically predicted internal resistance is slightly lower than the one measured experimentally. The ratio of these two resistances slightly decreases as the temperature difference is increased.

For the Hi-Z TEG modules, the manufacturer's model showed good agreement with the proposed model for the HZ-2 module. As for HZ-14 module, which has a larger surface area on sides, the predicted values using the one-dimensional model were in better agreement with the manufacturer's model over the low temperature difference region. Sensitivity analysis was then performed to examine the dependence of the output power on variations in the model parameters. Because of the large number of input parameters, this analysis had to performed independently on some of these parameters. This procedure could not address any correlation between these parameters that would impact the output power.

Chapter 3

Integration of TEG with an Organic Storage Device

3.1 Introduction

A thermoelectric generator converts thermal energy into electrical energy with a potential application in energy recovery from waste heat to power sensors or charge batteries. Ismail et al. [41] suggested that TEG can improve efficiencies of energy conversion systems by converting waste heat into electrical power. Kristiansen et al. [42] developed a mathematical model for TEG to predict the power harvested from marine incinerator used to burn liquid and solid waste. A seawater heat sink was used to maintain the temperature difference required for using the TEG. Their results showed a reduction in the cost per Watt. Samson et al. [43] installed a TEG on an air-

craft and tested it during flights. Based on the flight test, the tested TEG showed high reliability for harvesting energy. TEG has also been suggested for waste heat recovery from automobiles. Hsiao et al. [44] investigated heat recovery of internal combustion engine using thermoelectric generators. Exhaust gas and radiator were sources of heat. An optimum location for placing the TEG that produces high levels of power was the exhaust. The maximum power harvested was 0.43 W for a temperature difference of 290 K. Weilguni et al. [45] replaced engine alternator by implementing TEG modules. This feasibility study showed that 8,330 kWh can be harvested in 8 years of vehicles life. Liang et al. [46] developed an analytical model for parallel TEG based on conservation of energy, thermodynamics theory and semiconductor thermoelectric theory. They investigated their model and validated it experimentally. They concluded that the performance improved when the thermal contact resistance is reduced. Hsu et al. [28] investigated the power gained from automobile exhaust using 24 TEGs modules. To increase the temperature gradient, the cold side of each module was attached to a heat sink and a fan. The maximum power harvested was 12.41 W at a temperature difference of 30 K while the engine was operational at 3500 RPM. Optimum resistance which produced the maximum power was found between 23 and 30 W. Wang et al. [47] presented two-stage TEG design with an air-cooling system. The power harvested was improved by optimizing the heat sink used on cold side.

The performance of TEG can be significantly improved if they are integrated with an energy storage device. Capacitors are widely used in electronics appliances. However, organic storage devices can be a good replacement due to their low cost, high speed and simple fabrication. Organic storage devices (organic capacitors), similar to metal-insulator-semiconductor (MIS) structured

devices, contain charging elements (nanoparticles), insulator and semiconductors sandwiched between conductive electrodes. Haik et al. [48] developed an organic storage device which used Au-Pt-Ag nanoparticles as charge storage elements. Their results showed large capacitance-voltage hysteresis loops that indicated storage within the nanoparticles when compared with a reference device that did not contain nanoparticles.

Sargentis et al. [49], Mabrook et al. [50], [51] and Guan et al. [52] showed that gold nanoparticles can be used as charging elements in fabricating MIS structured storage devices. All the above investigators were able to obtain comparative hysteresis window gate that showed gold nanoparticles are responsible for storing the generated charge. Other researchers also used different nanoparticles such as copper [53], carbon nanotubes [54] and germanium [55] in constructing storage devices.

In this study, the integration of an organic storage device with voltage generated by TEG is evaluated experimentally. This integration covers several conditions including steady and unsteady temperature gradients.

3.2 Device fabrication

The semiconducting polymer made by doping glycerol, that acts as a plasticizer, with two non-conducting polymers. The process of producing the organic polymer blend is discussed in [48]. Cadmium sulfide (CdS) nanoparticles used in this study were synthesized by chemical co-precipitation technique. The procedures of synthesizing the nanoparticles consisted of the following steps. First, 100 mL of 1 mM of cadmium chloride ($CdCl_2$) was added to 100 mL of sodium citrate dihydrate

and magnetically stirred for 10 minutes. To this solution, 100 mL of sodium sulfide nonahydrate was added and stirred for 15 minutes. The yellow precipitate obtained in washed three times with deionized water and dried at 60^oC.

Figure (3.1) shows SEM images for cadmium sulfide, CdS, nanoparticles the plot shows small clusters scattered over the substrate. The size distribution by volume was verified by using the Zeta analyzer, which showed an average diameter size of approximately 27 nm as shown in Figure (3.2). Figure (3.3) shows that the composition of the nanoparticles of the Cd and S elements weight percentage are, respectively 81.14 wt% and 18.86 wt%, with 2381 ray counts received. Therefore, $Cd_{81.14}S_{18.86}$ will be used to describe the correct composition of the nanoparticle. Figure (3.4) shows a schematic of the layer-by-layer setup of the organic storage device and an actual image of the device being tested.

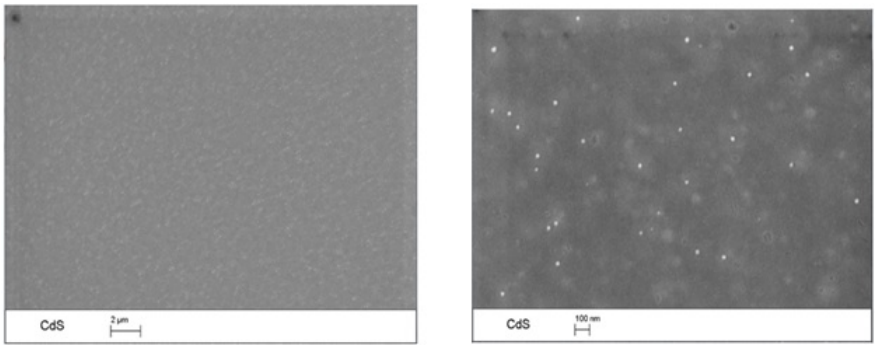

Figure 3.1: SEM images for CdS nanoparticles showing clusters over the substrate.

Capacitance-voltage (C-V) sweeps of the storage devices were performed using a Keithley 4200 semiconductor characterization system (SCS) computer controlled analyzer to investigate the charge storage that could be retained in the nanoparticles. The measurements were performed with a dual voltage sweep in the range of -20V to +20V and back to -20V at a scan rate of 0.5 V/s. This

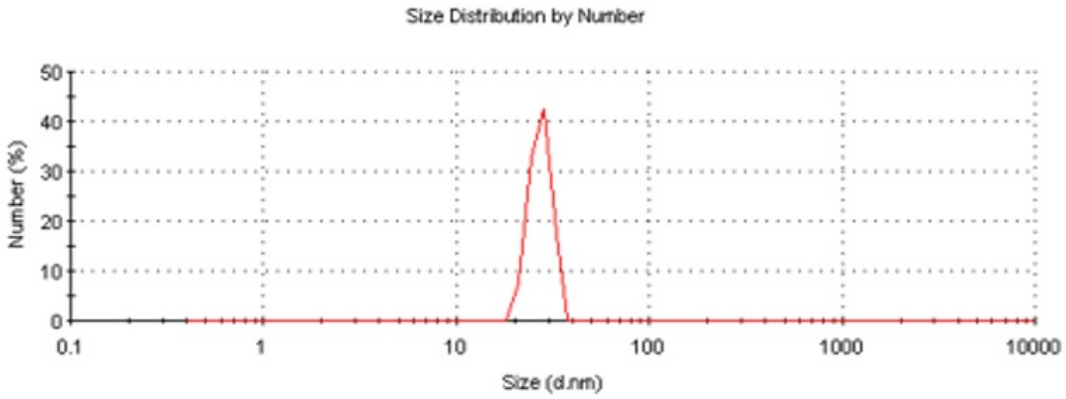

Figure 3.2: Zeta analyzer of CdS nanoparticles.

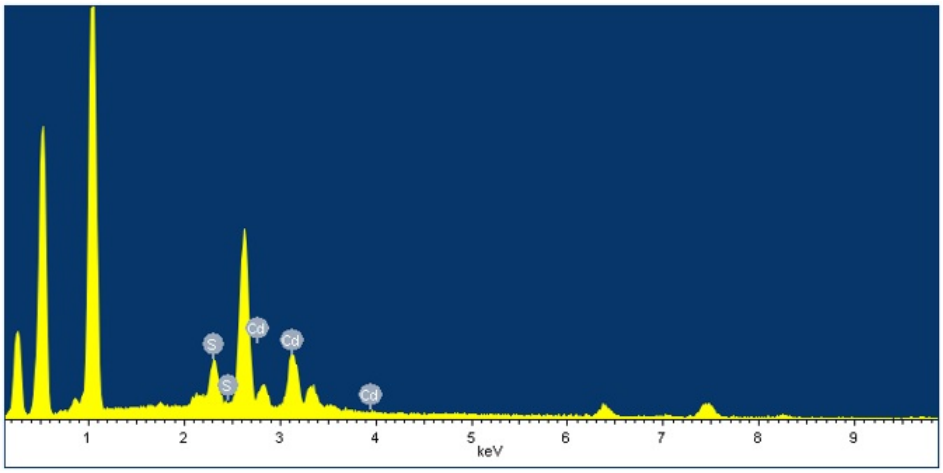

Figure 3.3: EDS spectra of CdS nanoparticles.

was done to show whether or not the devices can be used as charging elements by observing the presence or absence of any hysteresis loop and the width of the window gap as a function of the sweep range. The C-V measurements, plotted in Figure (3.5), shows the conventional accumulation (capacitor is charged) and inversion (capacitor is discharged) characteristics of a typical MIS device based on a p-type semiconductor [50].

The wide window gate observed in the hysteresis plots is a clear indication of the charge storage

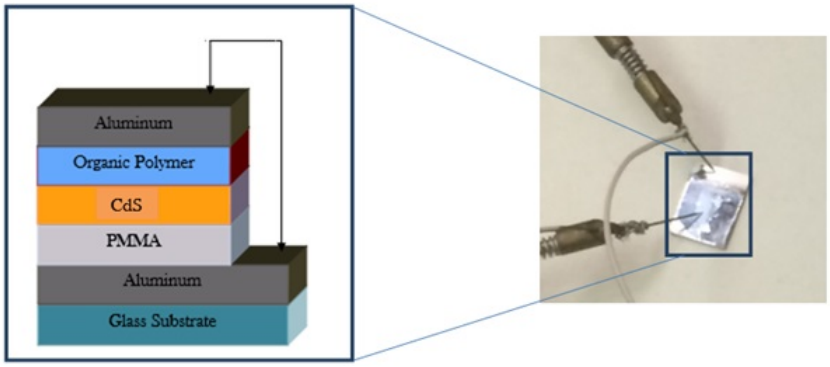

Figure 3.4: The layer-by-layer schematic of the device (left) and actual organic capacitor being tested (right).

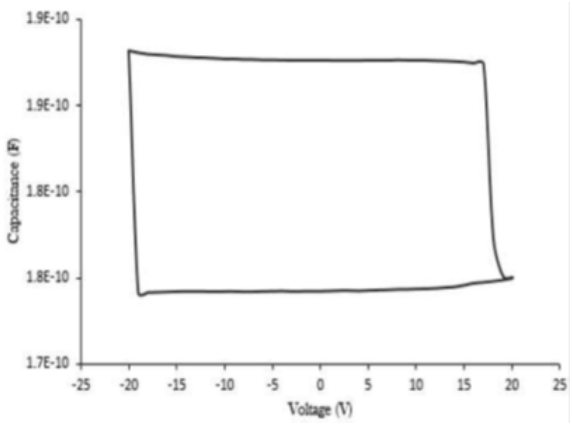

Figure 3.5: The C-V plot for Organic Memory Device.

capability within the nanoparticles. This large hysteresis window is mainly linked to the high charge transport mobility of the carriers. Because the reference device with no particles did not show a hysteresis with a window gap, it is concluded that the majority of the charge is being stored in the nanoparticles and not in the organic polymeric layer [56], [57] and [58].

3.3 Experimental setup

The Laird CP10,127,08 thermoelectric module was used to harvest energy. This module has 127 elements connected thermally in parallel and electrically in series. This TEG has square profile with a surface area of 30x30 mm^2 and a thickness of 4 mm. The organic capacitor consists of five layers. The aluminum electrode layers were thermally evaporated on a glass substrate with thickness of 100 nm. The glass substrate of dimensions 2 cm x 2 cm was used for handling purposes. After thermally evaporating the bottom electrode, the organic insulator, poly (methyl methacrylate) PMMA, was spun coated at 500 rmp for 10 seconds and then 5000 rpm for 50 s. This ensured uniform distribution of the insulating material. Then, the CdS storage elements were deposited on top of the PMMA layer by spin coating for one minute. The organic semiconduting polymer was later spun coated over the storage elements. After each spin coating process, the sample was heated over a hot plate set at 50^{o}C. Finally, the top aluminum electrode was thermally evaporated to a thickness of 100 nm.

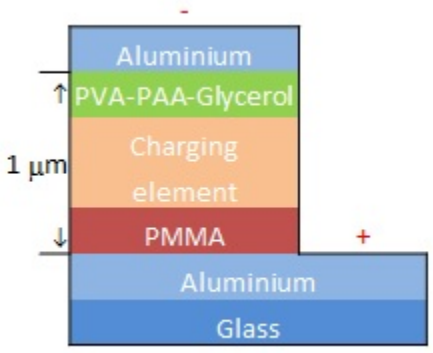

Figure 3.6: The schematic diagram of the organic capacitor.

An electrical hot plate is treated as the heat source for the TEG. The cold side was attached to a cold plate and a copper pipe was used to recycle water from a large tank to maintain constant cold temperature. Two K-type thermocouples were used to measure temperatures on both sides of the TEG.

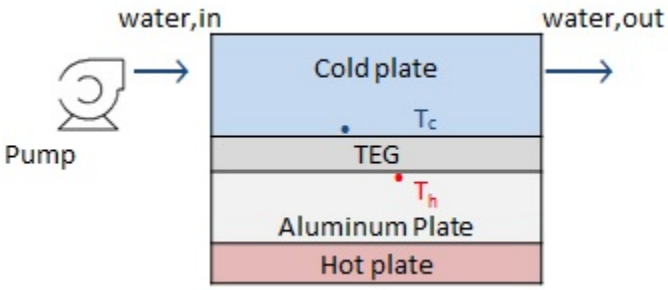

Figure 3.7: The experimental schematic diagram for the TEG setup.

The TEG was connected in series with the load resistance and the organic storage device. The data measured the voltage of the source, voltage across the organic capacitor and the temperature differences (ΔT). The voltage across the load is given by:

$$V_L = V_{TEG} - V_{cap} \tag{3.1}$$

where V_{TEG} is the output voltage from the TEG and V_{cap} is the voltage measured across the organic capacitor. The current in a series connection can be calculated using:

$$I = \frac{V_L}{R_L} = \frac{V_{TEG} - V_{cap}}{R_L} \tag{3.2}$$

where R_L is load resistance.

Two sets of experiments were performed. First, we raised the temperature of the hot plate for 20 minutes until reaching steady-state condition. The temperature difference is controlled by varying

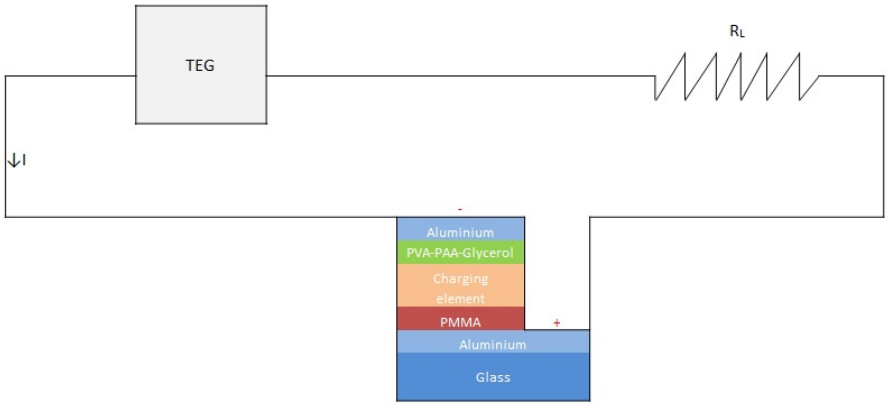

Figure 3.8: The experimental electrical circuit.

the temperature of the hot plate. The second, the TEG remains in steady-state condition for a seven minutes and then the TEG was cooled by turning off the heat source and record for 13 minutes. Four different load resistances 100, 200, 330 and 460 Ω, were used in each experimental set.

3.4 Results

Figures (3.9)-(3.12) show the variation of the current and voltage across the capacitor versus time, when the heating source was turned on and off for the load resistance values of 100, 200, 330 and 460 Ω, respectively. We should note here that the experimental growth and decay associated with the charging and discharging of the TEG is not only associated with the time constant of the capacitor. Rather, and because of the time variation of the heating source, the charging and discharging rates are associated with the heating and cooling rates of the hot plate. As such, we will consider here the impact of the load resistance and steady-state values of the hot temperature

on the charging density of the capacitor.

Figure (3.13) shows the variation in the steady-state current as a function of the temperature difference, ΔT, for different load resistances. It is interesting to note that the steady-state current varies linearly with the temperature difference. The highest slope is for the load resistance of 100 Ω. This indicates that, at this load resistance, the capacitor can achieve a higher charge value at a specific value of temperature difference. This also can bee seen in Figure (3.14), which shows the variations in the voltage across the capacitor as a function of temperature difference. For every value of temperature difference, the largest voltage is obtained for 100 Ωload resistance and decreases as the resistance is increased.

As shown in Figure (3.15), combining the results from the above figures shows that the internal resistance of the organic capacitor depends on the current. The low values of the load resistance lead to high values of the current which might have impacted the temperature of the capacitor itself and caused its resistance to increase significantly. So, in order, for the capacitor to charge, the right load resistance must be used. Values of voltage and current in Equations (3.1) and (3.2) has been averaged among steady-state condition.

The capacitance, C, of the capacitor is measured to be 100 nF. Also, the cross-sectional area of the capacitor, A_{cap}, is equal to 0.25 cm^2. Therefore, the average charge density can be expressed as:

$$\dot{q}_{charge} = \frac{CV_{cap}}{A_{cap}} \tag{3.3}$$

Figure (3.16) shows that the charge density is a function of the temperature difference and the load resistance. For the a specific value of temperature difference, the highest charge density is obtained

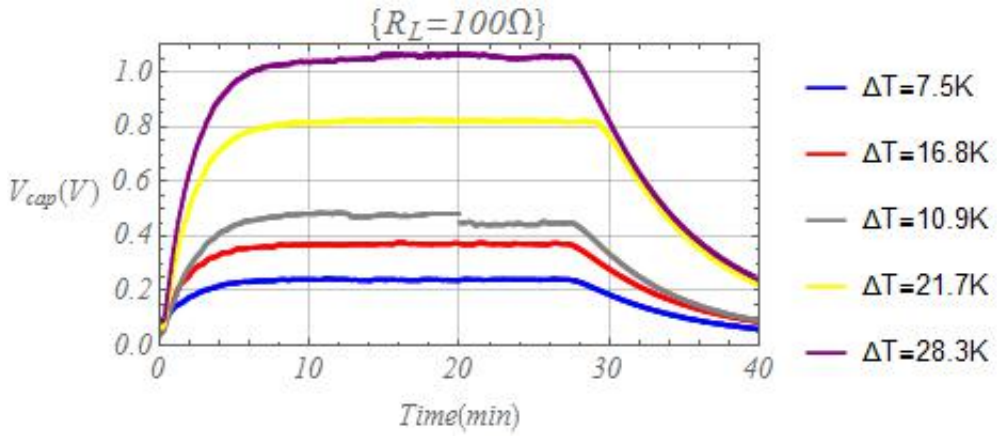

(a) The voltage across the organic capacitor versus time.

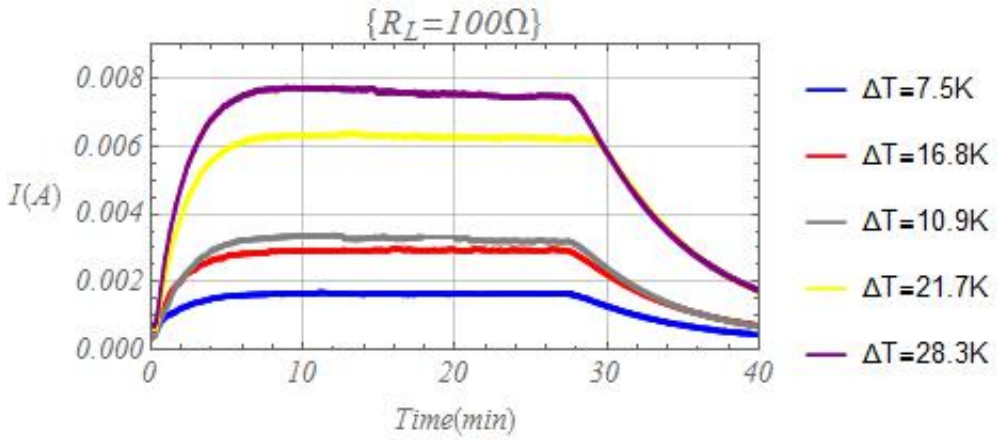

(b) The electrical circuit current versus time.

Figure 3.9: The experimental results with $R_L = 100\Omega$.

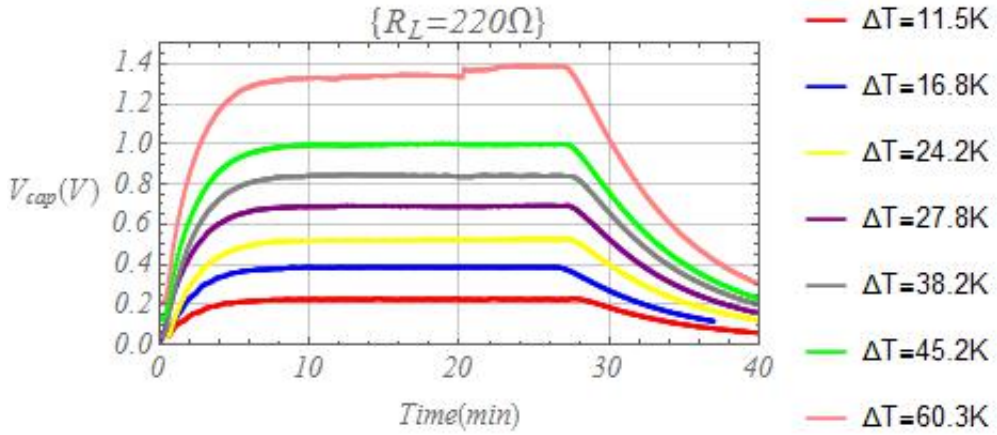

(a) The voltage across the organic capacitor versus time.

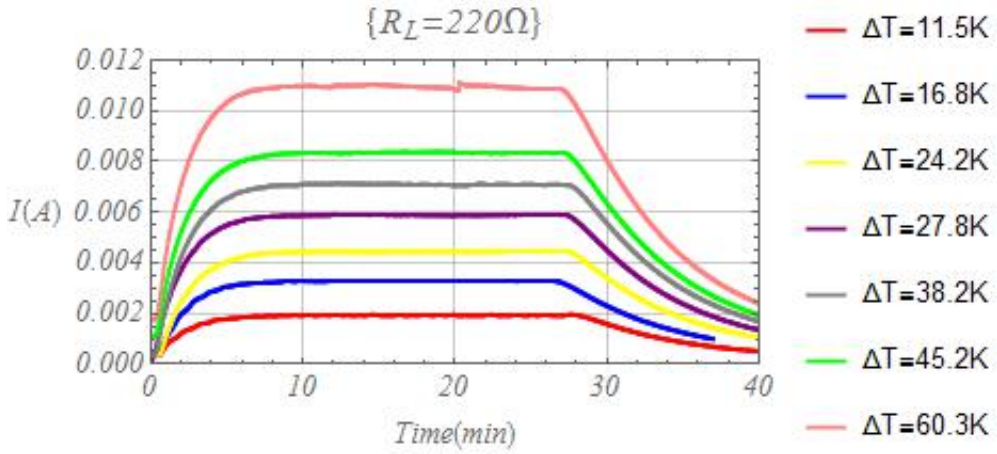

(b) The electrical circuit current versus time.

Figure 3.10: The experimental results with $R_L = 220\Omega$.

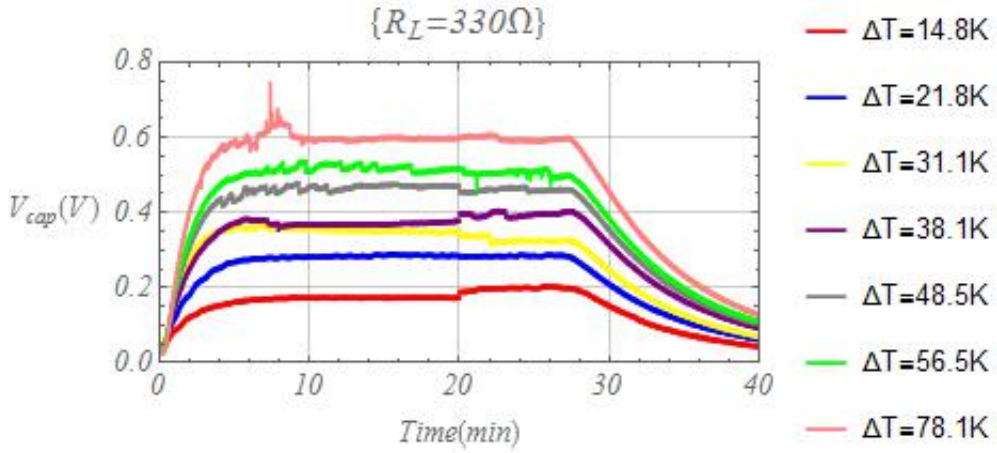

(a) The voltage across the organic capacitor versus time.

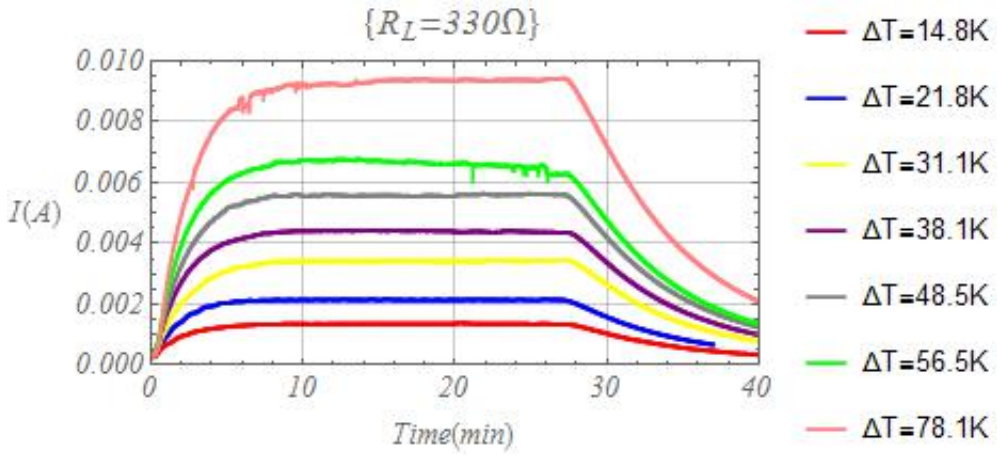

(b) The electrical circuit current versus time.

Figure 3.11: The experimental results with $R_L = 330\Omega$.

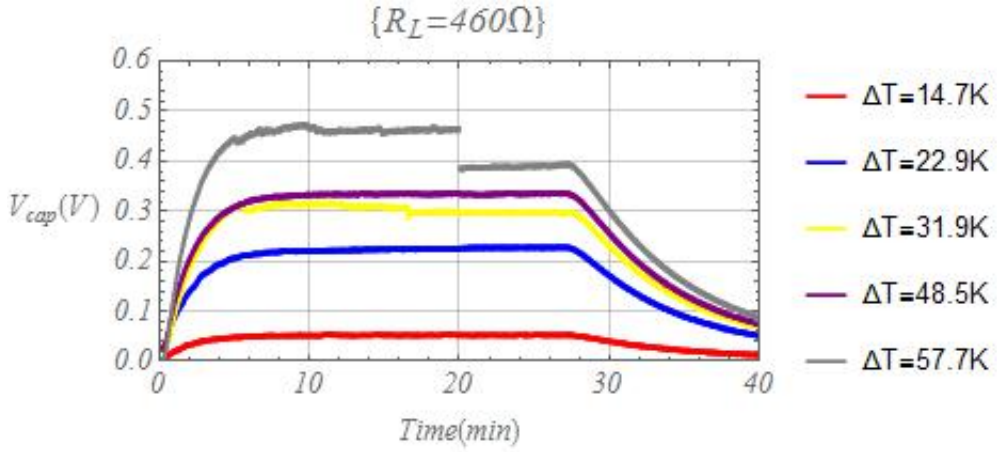

(a) The voltage across the organic capacitor versus time.

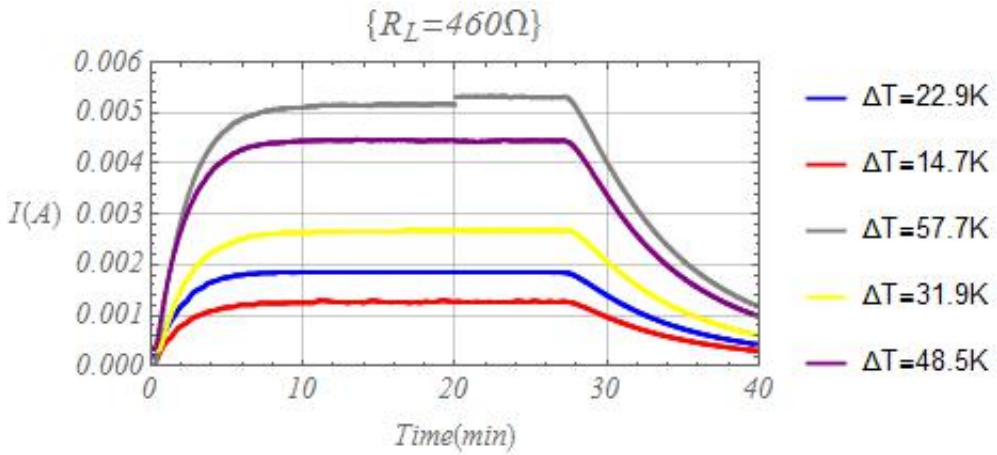

(b) The electrical circuit current versus time.

Figure 3.12: The experimental results with $R_L = 460\Omega$.

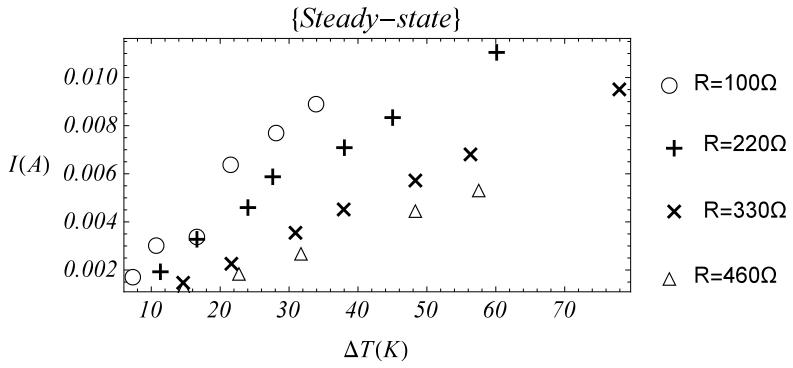

Figure 3.13: The average electrical circuit current versus temperature gradient at steady-state.

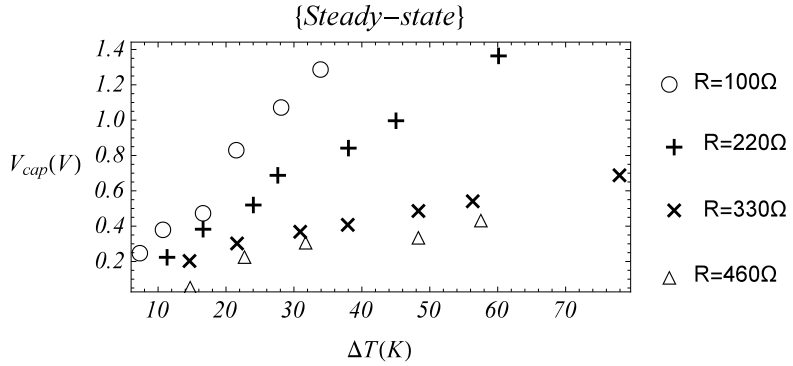

Figure 3.14: The average organic capacitor voltage versus temperature gradient at steady-state.

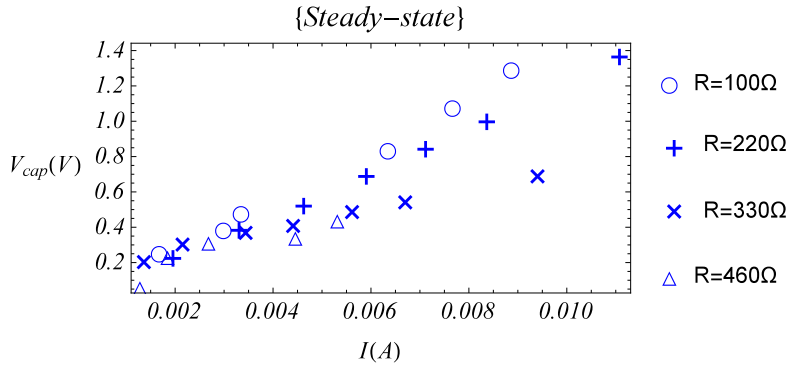

Figure 3.15: The average voltage across the organic capacitor versus average circuit current.

when the load resistance is 100 Ω. Particularity, a maximum charge density of 5.14 $\times 10^{-3} \frac{C}{m^2}$ is obtained for temperature difference of 34.1 K. Table (3.1) shows the reduction in charge density as the load resistance increased.

For a load resistance below 75 Ω, we did not detect measurable currents. A current was detected for resistance values that were larger than 100 Ω. At higher resistances the steady-state current decreased as the load resistance was increased. So, we tested it up to 460 Ω.

R_L	$\frac{d\dot{q}_{charge}}{d(\Delta T)}$	Reduction
(Ω)	(10^{-5})	$(\%)$
100	15	-
220	9	40
330	4	73.3
460	3	80

Table 3.1: The charge density reduction percentage with respect to load resistance.

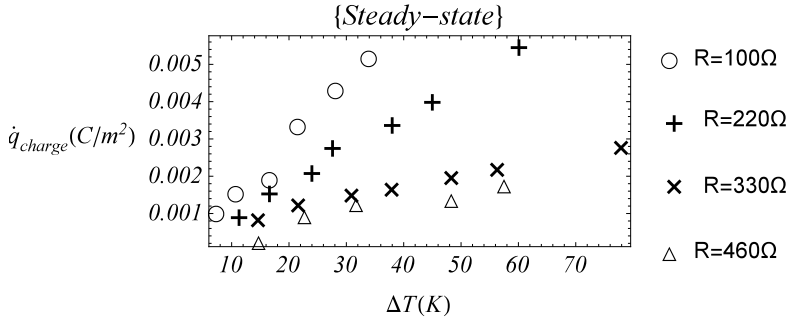

Figure 3.16: The average charge density versus temperature gradient.

3.5 Conclusions

We investigated the integration of a TEG module with an organic capacitor. The effect of the load resistance and steady-state values of the TEG's temperature difference on the charging density of the organic capacitor were investigated. The charging and discharging of the TEG are not associated with time constant of the capacitor. The circuit current and the temperature difference have a linear relationship. The value of the slope increases as the load resistance decreased. Also, a linear relation is found between the temperature difference and the voltage across the capacitor. The highest values of capacitor voltage for all temperature differences occur when the load resistance is 100 Ω. The organic capacitor internal resistance depends on the current of the circuit. The current value increased as the load resistance was decreased. The high values of electrical current could increase the temperature of the capacitor which, has an effect increasing the internal resistance of the capacitor. Therefore, a suitable load resistance should be used with the capacitor to be able to charge. For all temperature differences, the charging density of the capacitor rates were the highest at the 100 Ω load resistance. The reduction in charge density rates based on the highest values are 10 %, 60 % and 70 % for load resistances of 220 Ω, 330 Ω and 460 Ω, respectively.

Chapter 4

Use of TEG for Water Flow Metering

4.1 Introduction

Typical flow meters do not provide real-time monitoring of water use, i.e. metering. Water pipes are usually located behind walls or hard to reach places. Ideally, one would like to have a self-powered sensor that can measure and transmit data about the flow rate on a regular basis. The cost and placement of such sensors are relevant in dry areas where the levels of available water is low. These two aspects are not within the scope of this effort. Rather, we intend to show how a TEG can be used to measure hot water flow in a pipe with the expectation that harvested power can be used to send a signal about the water temperature and flow rate.

TEGs have been used to harvest power from water flow. Aranguren et al. [59] investigated harvesting energy from the wasted heat of hot water in heat exchanger using TEG. They showed that

the TEG gained power increased the increasing hot water mass flow rate of the hot water. Date et al. [60] studied TEGs power enhancement and optimization when integrated with a solar water heater. Lesage et al. [61] used two TEG modules to harvest power from the temperature difference between flow of hot and cold water channels. They explained both experimentally and numerically how turbulent velocity field in the channels can enhance the level of harvested power. Zhou et al. [62] proposed two methods to improve TEG modules performance that were placed between hot and cold water stream. The first method was to optimize the arrangement of TEG's elements along wall surfaces. The second method considered increasing the thermal conductivity of the water by loading CuO nanoparticles into water. Using both methods, the results showed a 30% increase in the level of harvested power.

The objective of this work is to use the harvested power to estimate the flow rate. Particularly, a mini TEG module is used as a flow meter by establishing a relationship between TEG's harvested power and the flow of hot water in a pipe. In the experimental setup, the hot water is delivered from a water heater that was insulated to maintained certain value of temperature. An Aluminum pipe is used. A non-dimensional relation is then established between the harvested peak power from the TEG and the Reynolds number.

4.2 Experimental setup

In the performed experiments, a mini TEG module was used to harvest electrical power from hot water flowing through a square pipe. As shown in Figure (4.1) the used TEG, Laird OT24,31,F1

has a base area of 10x10 mm^2 and 31 elements. It has a leg length of $0.01''$ and a height of $0.01''$. It was mounted on the surface of a 12 inches long square Aluminum pipe as shown in Figure (4.2). The pipe has a cross-section area of $3/4'' \times 3/4''$. Its thickness is $1/16''$. Both TEG's sides were covered with two Aluminum plates with a surface area of 10x10 mm^2 using thermal compound material. The plates had grooves where thermocouples were attached. Two K-type thermocouples were used to measure the TEG's hot and cold temperatures. The output voltage from the TEG module was connected to a 10 Ω load resistance. All data was taken by using a National Instruments data acquisition NI 9219 with sampling rate of 80 Hz. A picture of the experimental setup is presented in Figure (4.3).

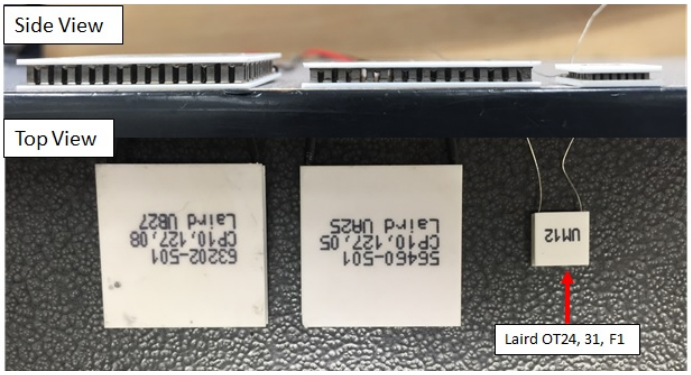

Figure 4.1: Three TEG modules: Laird CP10,08 , Laird CP10,05 and mini TEG module.

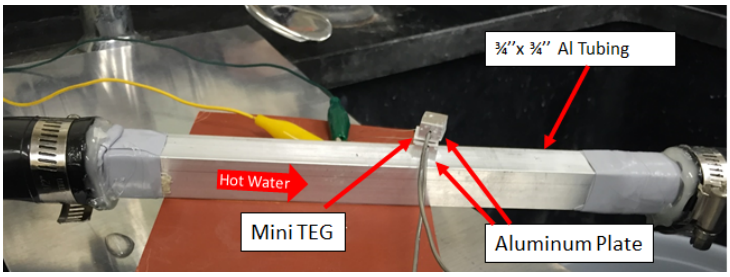

Figure 4.2: Picture of the TEG mounted on Al pipe.

The Aluminum pipe with the TEG module was attached to a faucet using suitable fittings and flexible hoses. The TEG module was placed seven inches away from pipe inlet. The hot water drained into a bucket where the water was collected. The volume of collected water and time used for its collection were used to determine the flow rate. Natural convection between the Aluminum plate on TEG's cold side and the ambient air temperature resulted in cooling the TEG.

The experiments were performed according to the following procedure. Data recording started right when the faucet was turned on. The data was taken for 10 minutes. After the first five minutes, the faucet was turned off. Data was then collected for another five minutes because the TEG continued to harvest power from the hot pipe. Experiments for different flow rates were performed.

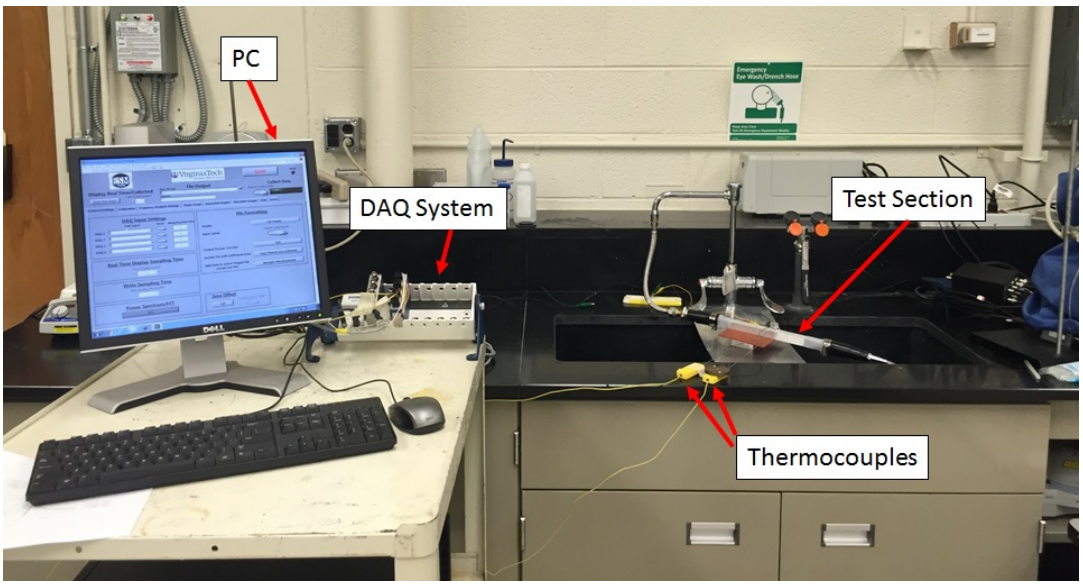

Figure 4.3: Picture of the experimental setup.

4.3 Results and Discussion

Two set of experiments were performed. In the first set, the ambient temperature was 19^oC and the average temperature of the water was 54.6^oC. In the second set, the ambient temperature was 22^oC and the average temperature of the water was 53.8^oC. Figure (4.4) shows the measured temperature difference with time over ten minutes. Clearly, a steady-state is reached after about three minutes. The observed drop after five minutes is due to shutting the water off. The harvested power is given by:

$$P_L(t) = \frac{V_L^2(t)}{R_L} \tag{4.1}$$

Figure (4.5) shows the measured voltage across the load resistance over the ten-minute period of each experiment. The results show that the voltage variations follow the temperature variations. Of interest is that the steady-state values obtained after three and eight minutes are independent of the flow rate. The reason is the that equilibrium conditions in terms of temperature variations across the TEG are independent of the flow rate. On the other hand, the initial rise in the measured voltage in terms of rate of voltage increase and peak value are a function of the flow rate. These differences are more pronounced, as shown in Figure (4.6), in the power variations because the power is proportional to the square of the voltage. As such, we propose to correlate the peak of the harvested power to the flow rate.

The mass flow rate in $(\frac{kg}{sec})$ is the product of water density, ρ ($985.65\ \frac{kg}{m^3}$) by the volume flow rate, Q:

$$\dot{m} = \rho Q \tag{4.2}$$

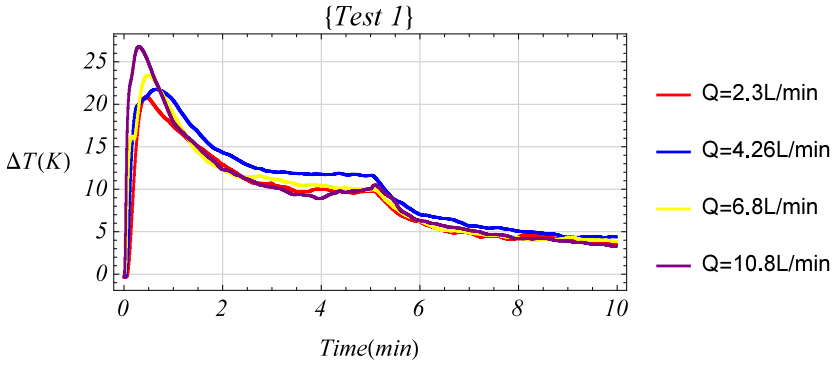

(a) Test 1.

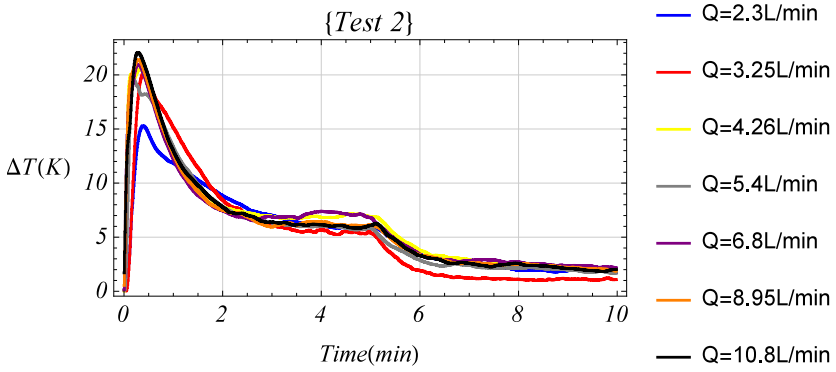

(b) Test 2.

Figure 4.4: Variation of the temperature difference with time for different flow rates.

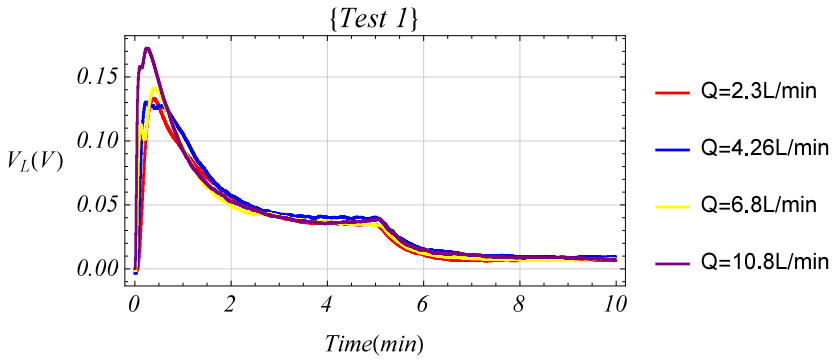

(a) Test 1.

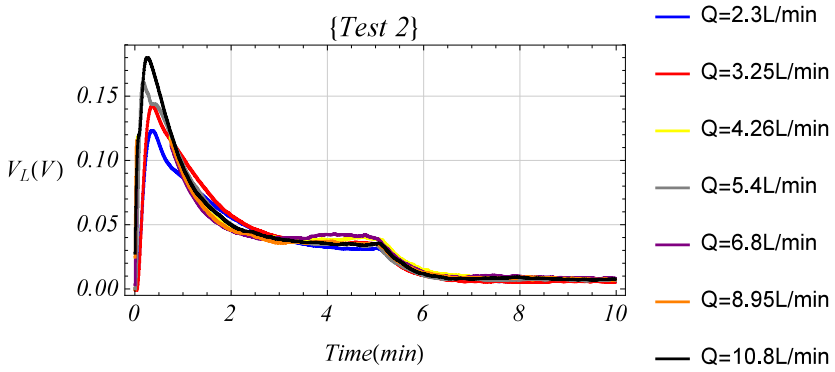

(b) Test 2.

Figure 4.5: The voltage across the load resistance versus time for different flow rates.

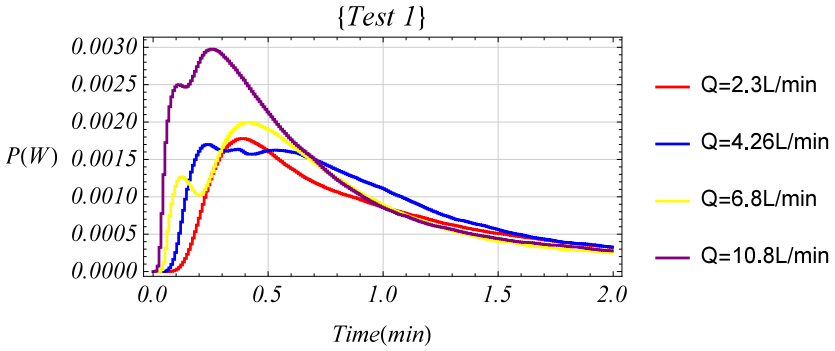

(a) Test 1.

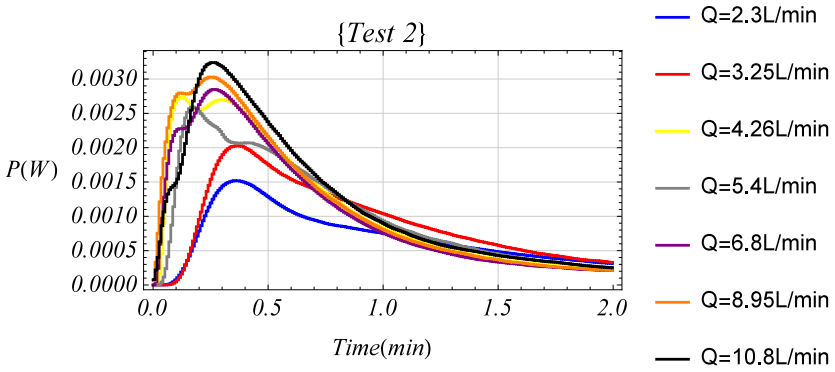

(b) Test 2.

Figure 4.6: The power output versus time for different flow rates for two minutes.

Figure (4.7) shows the maximum hot and cold temperatures across the TEG as a function of the flow rate. Although the hot temperature was more or less constant, the cold temperature showed slight variations; most likely because of small variations in the ambient temperature and natural convection. The maximum temperature difference as a function of the flow rate is shown in Figure (4.8). The plot shows small variations but with limited expected effects on the level of harvested power. Figure (4.9) shows the peak harvested power as a function of the flow rate. Clearly, the maximum harvested power increases as the flow rate increases. In comparison, we show in Figure (4.10) the harvested voltage under steady-state conditions. In addition to the measured data-points, we show predicted values from numerical simulations. The results show that the measured values are significantly lower than values predicted by numerical simulations because these simulations do not account for the natural convection, which based on these results, causes significant losses in the harvested voltage and power.

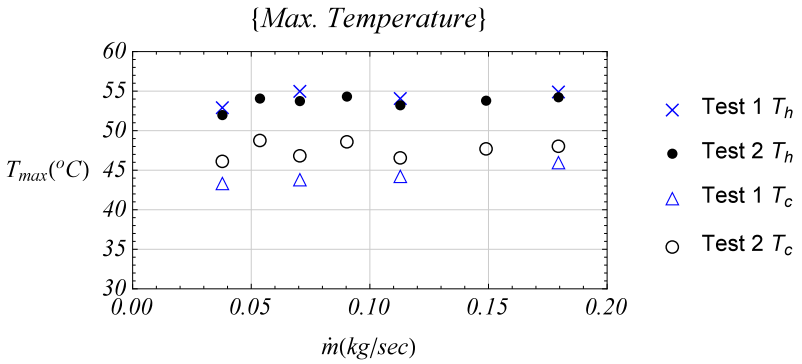

Figure 4.7: The maximum temperature versus mass flow rate.

The Reynolds number is directly related to the flow rate, Q, and given by:

$$Re = \frac{\rho V D_H}{\mu} = \frac{Q D_H}{\nu A} = \frac{Q}{\nu D_H} \tag{4.3}$$

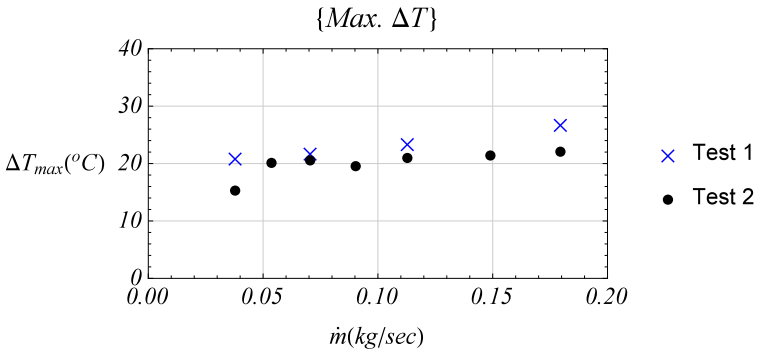

Figure 4.8: The maximum temperature difference versus mass flow rate.

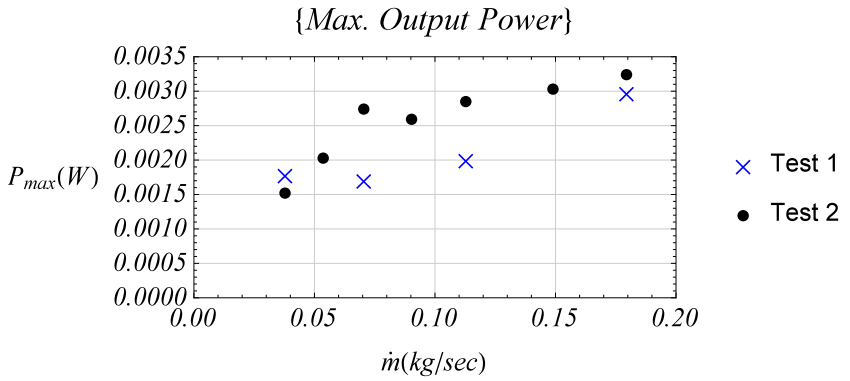

Figure 4.9: The maximum power harvested versus mass flow rate.

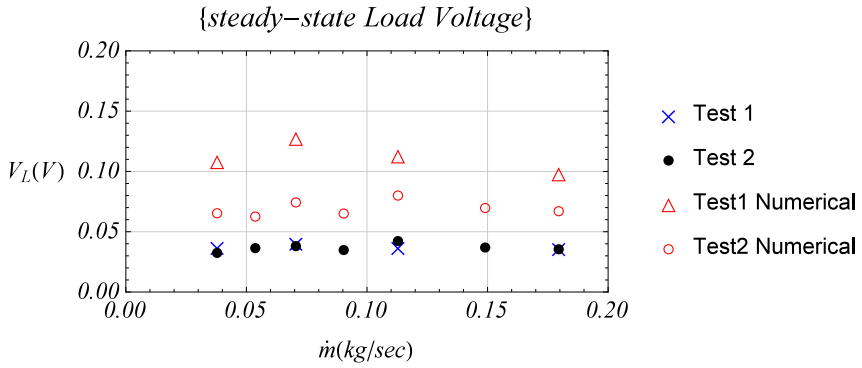

Figure 4.10: The voltage gained at steady state versus mass flow rate.

where D_H is the hydraulic diameter for the square aluminum pipe. The kinematic viscosity of water at 55^oC is equal to 0.514x10$^-$6$\frac{m^2}{Sec}$. By substituting Equation (4.2) into Equation (4.3), one obtains

$$Re = \frac{\dot{m}}{\rho \nu D_H} \tag{4.4}$$

Figure (4.11) shows the maximum harvested power as a function of the Reynolds number. The plot shows that this power increases as the Reynolds number is increased. As such, there is a good correlation between the harvested power and the flow rate. This correlation can be better represented by plotting the nondimensional power as function of the flow rate. The nondimensional power is defined by dividing the measured power by the heating rate from the flow of the hot water defined by:

$$\dot{q}_{heat} = \dot{m} c_p \Delta T \tag{4.5}$$

where c_p is the specific heat for water at 55^oC which is equal to 4182 $\frac{J}{Kkg}$. The temperature difference is given by:

$$\Delta T = T_{flow} - T_{amb} \tag{4.6}$$

A plot of the nondimensional maximum power as a function of the Reynolds number is presented in Figure (4.12). The plot shows that the nondimensional power decreases as the Reynolds number is increased with the relation between them approximated by:

$$\frac{P_{max}}{\dot{q}_{heat}} = 4.54 \times 10^{-5} Re^{-3/5} \tag{4.7}$$

This relation can be effectively used to estimate the flow rate from the level of harvested power.

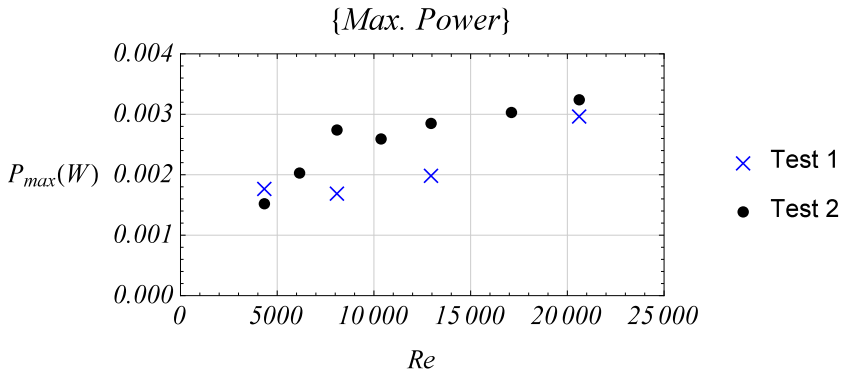

Figure 4.11: The maximum power gained versus Reynolds number.

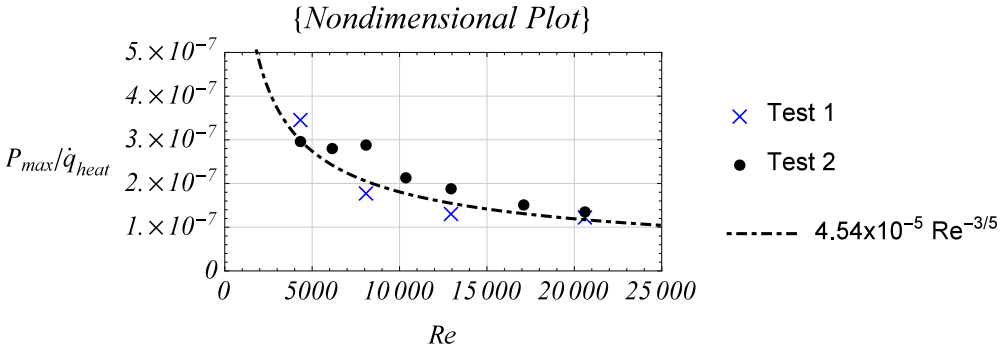

Figure 4.12: The ratio of maximum TEG power over the heat flux versus Reynolds number.

By substituting Equations (4.5) into left hand side of Equation (4.7) and (4.4) into the RHS of Equation (4.7), one obtains

$$\frac{P_{max}}{\dot{m}c_p\Delta T} = 4.54\times10^{-5}\left(\frac{\dot{m}}{\rho\nu D_H}\right)^{-3/5} \tag{4.8}$$

The mass flow rate in terms of the power is then approximated by:

$$\dot{m} = \left(\frac{P_{max}(\rho\nu D_H)^{-3/5}}{4.54\times10^{-5}c_p\Delta T}\right)^{5/2} \tag{4.9}$$

In case where the mini TEG module is attached the square aluminum pipe while hot water flowing through, the output maximum power from the TEG is P_{max} in Watt. The TEG connected electrically

in series with load resistance of 10 Ω. If the water heater is set to a maintain hot temperature of 54^oC, one can find the flow properties at this temperature as shown in Table (4.1). Given a the surrounding ambient temperature of 25^oC, the mass flow rate in Equation (4.9) can be approximated by:

$$\dot{m} = 510.97 \times 10^3 P_{max}^{5/2} \tag{4.10}$$

Property	Value
$\rho(\frac{kg}{m^3})$	985.65
$\nu(\frac{m^2}{sec}) \times 10^{-6}$	0.514
$c_p(\frac{J}{kg.K})$	4182

Table 4.1: The properties of water at 55^oC.

4.4 Conclusions

Through this experiment, we have shown how a TEG can be used to measure the flow rate of hot water. A non-dimensional fitting formula was established to relate the electrical to heat energy and Reynolds number. Through this step the TEG can be used as a self-powered monitoring device to transfer data about water flow rate in a pipe.

Chapter 5

Conclusions and Future Recommendations

The findings of this dissertation can be summarized as follows:

1) A simplified one-dimensional model for predicting TEG power output was developed and validated. Issues related to its predicted values over specific ranges of geometric dimensions (leg height and aspect ratio) and operating temperature differences were identified. The employed iteration procedure should be verified in future work and for higher fidelity models.

2) A commercial TEG was integrated with an organic storage device. The potential of using such an integrated system over a wide range of operating temperature differences and load resistances was evaluated. These results are encouraging and further parametric studies are recommended.

3) A new concept for using the TEG to determine the flow rate of hot water in a pipe was experimentally tested. A formula relating the maximum output power to the flow rate was established. Further tests with different pipe material and over broader ranges of flow rates and temperatures are recommended.

Bibliography

[1] L. Anatychuk, Y. Rozver, and D. Velichuk, "Thermoelectric generator for a stationary diesel plant," *Journal of Electronic Materials*, vol. 40, no. 5, pp. 1206–1208, 2011.

[2] A. Elefsiniotis, T. Becker, and U. Schmid, "Thermoelectric energy harvesting using phase change materials (pcms) in high temperature environments in aircraft," *Journal of Electronic Materials*, vol. 43, no. 6, pp. 1809–1814, 2014.

[3] A. Elefsiniotis, N. Kokorakis, T. Becker, and U. Schmid, "A thermoelectric-based energy harvesting module with extended operational temperature range for powering autonomous wireless sensor nodes in aircraft," *Sensors and Actuators A: Physical*, vol. 206, no. 0, pp. 159 – 164, 2014.

[4] B. Xiong, L. Chen, F. Meng, and F. Sun, "Modeling and performance analysis of a two-stage thermoelectric energy harvesting system from blast furnace slag water waste heat," *Energy*, vol. 77, no. 0, pp. 562 – 569, 2014.

[5] X. Liu, Y. Deng, Z. Li, and C. Su, "Performance analysis of a waste heat recovery thermo-

electric generation system for automotive application," *Energy Conversion and Management*, vol. 90, no. 0, pp. 121 – 127, 2015.

[6] X. Sun, X. Liang, G. Shu, H. Tian, H. Wei, and X. Wang, "Comparison of the two-stage and traditional single-stage thermoelectric generator in recovering the waste heat of the high temperature exhaust gas of internal combustion engine," *Energy*, vol. 77, no. 0, pp. 489 – 498, 2014.

[7] M. Cino, *Design and Implementation of an Extensive Test Facility for Thermoelectric Materials and Devices*. McMaster University, Hamilton, Ontario: Pergmon Press, second ed., 2014.

[8] X.-D. Wang, Y.-X. Huang, C.-H. Cheng, D. T.-W. Lin, and C.-H. Kang, "A three-dimensional numerical modeling of thermoelectric device with consideration of coupling of temperature field and electric potential field," *Energy*, vol. 47, no. 1, pp. 488 – 497, 2012. Asia-Pacific Forum on Renewable Energy 2011.

[9] J.-H. Meng, X.-X. Zhang, and X.-D. Wang, "Characteristics analysis and parametric study of a thermoelectric generator by considering variable material properties and heat losses," *International Journal of Heat and Mass Transfer*, vol. 80, no. 0, pp. 227 – 235, 2015.

[10] X.-D. Wang, Q.-H. Wang, and J.-L. Xu, "Performance analysis of two-stage tecs (thermoelectric coolers) using a three-dimensional heat-electricity coupled model," *Energy*, vol. 65, no. 0, pp. 419 – 429, 2014.

[11] R. McCarty, "A comparison between numerical and simplified thermoelectric cooler models," *Journal of Electronic Materials*, vol. 39, no. 9, pp. 1842–1847, 2010.

[12] M. Chen, L. A. Rosendahl, and T. Condra, "A three-dimensional numerical model of thermoelectric generators in fluid power systems," *International Journal of Heat and Mass Transfer*, vol. 54, no. 13, pp. 345 – 355, 2011.

[13] L. Gaowei, Z. Jiemin, and H. Xuezhang, "Output characteristics analysis of thermoelectric generator based on accurate numerical model," pp. 1–4, March 2010.

[14] Y. Yang, N. Wang, G. Dong, Y. Liu, B. Chen, J. Xue, H. Shan, and Y. Zhang, "Two-dimensional electrical modeling of thermoelectric devices considering temperature-dependent parameters under the condition of nonuniform substrate temperature distribution," *Microelectronics Journal*, vol. 44, no. 3, pp. 270 – 276, 2013.

[15] B. Reddy, M. Barry, J. Li, and M. K. Chyu, "Thermoelectric-hydraulic performance of a multistage integrated thermoelectric power generator," *Energy Conversion and Management*, vol. 77, no. 0, pp. 458 – 468, 2014.

[16] A. Z. Sahin and B. S. Yilbas, "Thermodynamic irreversibility and performance characteristics of thermoelectric power generator," *Energy*, vol. 55, no. 0, pp. 899 – 904, 2013.

[17] R. Bjok, D. Christensen, D. Eriksen, and N. Pryds, "Analysis of the internal heat losses in a thermoelectric generator," *International Journal of Thermal Sciences*, vol. 85, no. 0, pp. 12 – 20, 2014.

[18] A. Morega, M. Morega, and M. Panait, "Structural optimization of a thermoelectric generator by numerical simulation," *lectrotechnique et lectronergtique*, vol. 55, no. 1, pp. 3 – 12, 2010.

[19] H. Fateh, C. A. Baker, M. J. Hall, and L. Shi, "High fidelity finite difference model for exploring multi-parameter thermoelectric generator design space," *Applied Energy*, vol. 129, no. 0, pp. 373 – 383, 2014.

[20] F. Meng, L. Chen, and F. Sun, "A numerical model and comparative investigation of a thermoelectric generator with multi-irreversibilities," *Energy*, vol. 36, no. 5, pp. 3513 – 3522, 2011.

[21] T. Ming, Y. Wu, C. Peng, and Y. Tao, "Thermal analysis on a segmented thermoelectric generator," *Energy*, vol. 80, no. 0, pp. 388 – 399, 2015.

[22] M. Zhou, Y. He, and Y. Chen, "A heat transfer numerical model for thermoelectric generator with cylindrical shell and straight fins under steady-state conditions," *Applied Thermal Engineering*, vol. 68, no. 12, pp. 80 – 91, 2014.

[23] M. Chen, L. Rosendahl, I. Bach, T. Condra, and J. Pedersen, "Transient behavior study of thermoelectric generators through an electro-thermal model using spice," in *Thermoelectrics, 2006. ICT '06. 25th International Conference on*, pp. 214–219, Aug 2006.

[24] K. J. Kim, "Thermal and power generating performances of thermoelectric energy recovery modules," in *Thermal and Thermomechanical Phenomena in Electronic Systems (ITherm), 2010 12th IEEE Intersociety Conference on*, pp. 1–7, June 2010.

[25] L. L. Baranowski, G. Jeffrey Snyder, and E. S. Toberer, "Effective thermal conductivity in thermoelectric materials," *Journal of Applied Physics*, vol. 113, no. 20, 2013.

[26] H. Lee, A. M. Attar, and S. L. Weera, "Performance prediction of commercial thermoelectric cooler modules using the effective material properties," *Journal of Electronic Materials*, vol. 44, no. 6, pp. 2157–2165, 2015.

[27] S. Kim, "Analysis and modeling of effective temperature differences and electrical parameters of thermoelectric generators," *Applied Energy*, vol. 102, pp. 1458 – 1463, 2013.

[28] C.-T. Hsu, G.-Y. Huang, H.-S. Chu, B. Yu, and D.-J. Yao, "Experiments and simulations on low-temperature waste heat harvesting system by thermoelectric power generators," *Applied Energy*, vol. 88, no. 4, pp. 1291 – 1297, 2011.

[29] H.-C. Chien, E.-T. Chu, H.-L. Hsieh, J.-Y. Huang, S.-T. Wu, M.-J. Dai, C.-K. Liu, and D.-J. Yao, "Evaluation of temperature-dependent effective material properties and performance of a thermoelectric module," *Journal of Electronic Materials*, vol. 42, no. 7, pp. 2362–2370, 2013.

[30] C. Su, W. Wang, X. Liu, and Y. Deng, "Simulation and experimental study on thermal optimization of the heat exchanger for automotive exhaust-based thermoelectric generators," *Case Studies in Thermal Engineering*, vol. 4, pp. 85 – 91, 2014.

[31] J.-Y. Jang and Y.-C. Tsai, "Optimization of thermoelectric generator module spacing and spreader thickness used in a waste heat recovery system," *Applied Thermal Engineering*, vol. 51, no. 12, pp. 677 – 689, 2013.

[32] W. He, S. Wang, X. Zhang, Y. Li, and C. Lu, "Optimization design method of thermoelectric generator based on exhaust gas parameters for recovery of engine waste heat," *Energy*, vol. 91, pp. 1 – 9, 2015.

[33] J.-H. Meng, X.-X. Zhang, and X.-D. Wang, "Multi-objective and multi-parameter optimization of a thermoelectric generator module," *Energy*, vol. 71, pp. 367 – 376, 2014.

[34] H. Tian, X. Sun, Q. Jia, X. Liang, G. Shu, and X. Wang, "Comparison and parameter optimization of a segmented thermoelectric generator by using the high temperature exhaust of a diesel engine," *Energy*, vol. 84, pp. 121 – 130, 2015.

[35] C. Favarel, J.-P. Bdcarrats, T. Kousksou, and D. Champier, "Numerical optimization of the occupancy rate of thermoelectric generators to produce the highest electrical power," *Energy*, vol. 68, pp. 104 – 116, 2014.

[36] X. Gao, S. J. Andreasen, S. K. Kaer, and L. A. Rosendahl, "Optimization of a thermoelectric generator subsystem for high temperature PEM fuel cell exhaust heat recovery," *International Journal of Hydrogen Energy*, vol. 39, no. 12, pp. 6637 – 6645, 2014.

[37] C.-T. Hsu, G.-Y. Huang, H.-S. Chu, B. Yu, and D.-J. Yao, "An effective seebeck coefficient obtained by experimental results of a thermoelectric generator module," *Applied Energy*, vol. 88, no. 12, pp. 5173 – 5179, 2011.

[38] A. Abdelkefi, A. Alothman, and M. Hajj, "Performance analysis and validation of thermoelectric energy harvesters," *SMART MATERIALS AND STRUCTURES*, vol. 22, Sep 2013.

[39] L. E. Landau L.D., *Elecrodynamics of continuous media*. Oxford, UK: Pergmon Press, second ed., 1960.

[40] Hi-Z Technology Inc., "Hi-z module performance," Nov. 2015.

[41] B. I. Ismail and W. H. Ahmed, "Thermoelectric power generation using waste-heat energy as an alternative green technology," *Recent Patents on Electrical Engineering*, vol. 2, no. 1, pp. 27–39, 2009.

[42] N. Kristiansen, G. Snyder, H. Nielsen, and L. Rosendahl, "Waste heat recovery from a marine waste incinerator using a thermoelectric generator," *Journal of ELECTRONIC MATERIALS*, vol. 41, no. 6, pp. 1024–1029, 2012.

[43] D. Samson, M. Kluge, T. Fuss, U. Schmid, and T. Becker, "Flight test results of a thermoelectric energy harvester for aircraft," *Journal of ELECTRONIC MATERIALS*, vol. 41, no. 6, pp. 1134–1137, 2012.

[44] Y. Hsiao, W. Chang, and S. Chen, "A mathematic model of thermoelectric module with applications on waste heat recovery from automobile engine," *Energy*, vol. 35, no. 3, pp. 1447 – 1454, 2010.

[45] M. Weilguni, M. Franz, and N. Slyusar, "Feasibility study and life cycle energy balance of thermoelectric generator modules for automotive applications," pp. 355–359, May 2012.

[46] G. Liang, J. Zhou, and X. Huang, "Analytical model of parallel thermoelectric generator," *Applied Energy*, vol. 88, no. 12, pp. 5193 – 5199, 2011.

[47] C.-C. Wang, C.-I. Hung, and W.-H. Chen, "Design of heat sink for improving the performance of thermoelectric generator using two-stage optimization," *Energy*, vol. 39, no. 1, pp. 236 – 245, 2012. Sustainable Energy and Environmental Protection 2010.

[48] M. Y. Haik, A. I. Ayesh, T. Abdulrehman, and Y. Haik, "Novel organic memory devices using auptag nanoparticles as charge storage elements," *Materials Letters*, vol. 124, no. 0, pp. 67 – 72, 2014.

[49] C. Sargentis, K. Giannakopoulos, A. Travlos, and D. Tsamakis, "Fabrication and electrical characterization of a MOS memory device containing self-assembled metallic nanoparticles," *Physica E: Low-dimensional Systems and Nanostructures*, vol. 38, no. 12, pp. 85 – 88, 2007. Proceedings of the E-MRS 2006 Symposium C: Silicon Nanocrystals for Electronic and Sensing Applications.

[50] M. Mabrook, Y. Yun, C. Pearson, D. Zeze, and M. Petty, "A pentacene-based organic thin film memory transistor," *Applied Physics Letters*, vol. 94, p. 173302, Apr. 2009.

[51] M. F. Mabrook, C. Pearson, D. Kolb, D. A. Zeze, and M. C. Petty, "Memory effects in hybrid silicon-metallic nanoparticle-organic thin film structures," *Organic Electronics*, vol. 9, no. 5, pp. 816 – 820, 2008.

[52] W. Guan, S. Long, M. Liu, Z. Li, Y. Hu, and Q. Liu, "Fabrication and charging characteristics of mos capacitor structure with metal nanocrystals embedded in gate oxide," *Journal of Physics D: Applied Physics*, vol. 40, no. 9, p. 2754, 2007.

[53] R. K. Gupta, D. Y. Kusuma, P. Lee, and M. Srinivasan, "Copper nanoparticles embedded in a polyimide film for non-volatile memory applications," *Materials Letters*, vol. 68, no. 0, pp. 287 – 289, 2012.

[54] A. Sleiman, M. Rosamond, M. A. Martin, A. Ayesh, A. A. Ghaferi, A. Gallant, M. Mabrook, and D. Zeze, "Pentacene-based metal-insulator-semiconductor memory structures utilizing single walled carbon nanotubes as a nanofloating gate.," *Applied physics letters.*, vol. 100, p. 023302, January 2012.

[55] S. Duguay, S. Burignat, P. Kern, J. J. Grob, A. Souifi, and A. Slaoui, "Retention in metalox-idesemiconductor structures with two embedded self-aligned ge-nanocrystal layers," *Semiconductor Science and Technology*, vol. 22, no. 8, p. 837, 2007.

[56] Y.-H. Kim, M. Kim, S. Oh, H. Jung, Y. Kim, T.-S. Yoon, Y.-S. Kim, and H. Ho Lee, "Organic memory device with polyaniline nanoparticles embedded as charging elements," *Applied Physics Letters*, vol. 100, no. 16, 2012.

[57] D. I. Son, D. H. Park, J. B. Kim, J.-W. Choi, T. W. Kim, B. Angadi, Y. Yi, and W. K. Choi, "Bistable organic memory device with gold nanoparticles embedded in a conducting poly(n-vinylcarbazole) colloids hybrid," *The Journal of Physical Chemistry C*, vol. 115, no. 5, pp. 2341–2348, 2011.

[58] Q. Shi, J. Xu, Y. Wu, Y. Wang, X. Wang, Y. Hong, L. Jiang, and L. Li, "Electrical bistable properties of hybrid device based on sio2 modified-zno nanoparticles embedded in poly-4-vinyl-phenol," *Physics Letters A*, vol. 378, no. 47, pp. 3544 – 3548, 2014.

[59] P. Aranguren, D. Astrain, and M. G. Prez, "Computational and experimental study of a complete heat dissipation system using water as heat carrier placed on a thermoelectric generator," *Energy*, vol. 74, pp. 346 – 358, 2014.

[60] A. Date, A. Date, C. Dixon, and A. Akbarzadeh, "Theoretical and experimental study on heat pipe cooled thermoelectric generators with water heating using concentrated solar thermal energy," *Solar Energy*, vol. 105, pp. 656 – 668, 2014.

[61] F. J. Lesage, E. V. Sempels, and N. Lalande-Bertrand, "A study on heat transfer enhancement using flow channel inserts for thermoelectric power generation," *Energy Conversion and Management*, vol. 75, pp. 532 – 541, 2013.

[62] S. Zhou, B. G. Sammakia, B. White, P. Borgesen, and C. Chen, "Enhancement of the power-conversion efficiency for thermoelectric generators," *ASME 2013 International Technical Conference and Exhibition on Packaging and Integration of Electronic and Photonic Microsystems*, vol. 1, p. 8, 2014.